POLITECNICO DI TORINO

SCUOLA DI DOTTORATO

Dottorato in Fluidodinamica – XXI Ciclo

Tesi di Dottorato
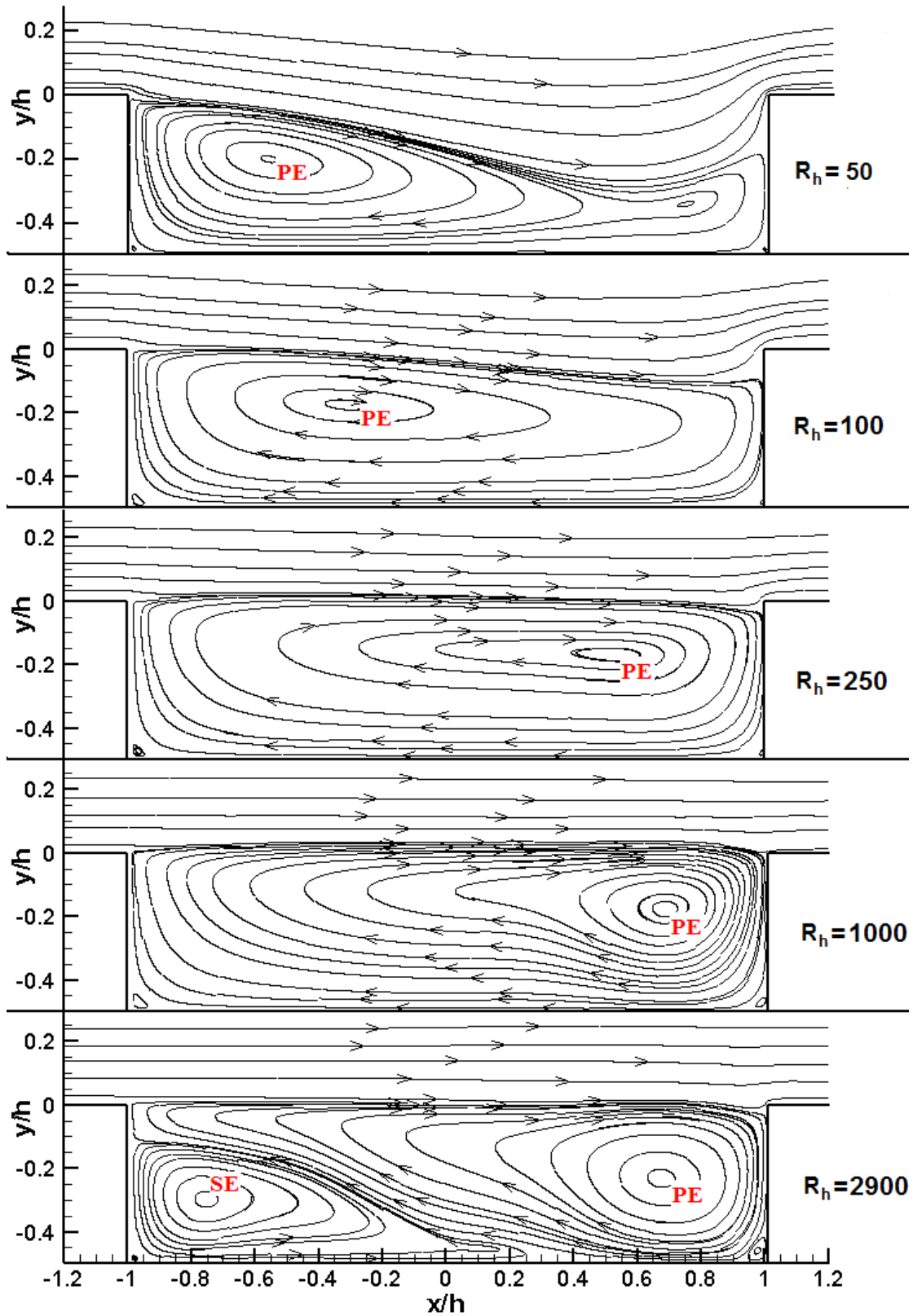

Reynolds number dependence of pressure velocity interaction in recirculatory flows

Peter Bailey

Tutor Prof. Daniela Tordella

February 2009

Reynolds number dependence of pressure velocity interaction in recirculatory flows

Contents

1. Introduction

Recirculation zones can be found in many natural and engineering contexts. In both turbulent and laminar flows, separation, caused by a sudden change in geometry or a strong adverse pressure gradient, induces vortex formation, which can be either steady or unsteady. The energy balance changes dramatically in these configurations when compared to flows which are predominantly uni-directional, such as a plane channel flow or boundary layer, affecting the flow dynamics and inducing greater mixing and transport phenomena. The study of this increased flow complexity is important in order to be able to understand better the interactions between, and the dispersion of the flow properties. This knowledge is key to developing and improving models designed for problems which include recirculatory phenomena.

Observing the kinetic energy transport statistics of wall bounded flows it can be seen that the dominant terms are the production and viscous dissipation, followed by its viscous diffusion and the turbulent transport. This differs in recirculation zones, where Le, Moin and Kim (1997) (LMK) and Yoshizawa (1982, 2002) have highlighted the redistribution of the energy for turbulent flows, such as those downstream of backsteps. Although still dominated by kinetic energy production and viscous dissipation, there is a rearrangement of the relative importance between the other terms, specifically the pressure transport represents a greater proportion of the kinetic energy transport. This was brought to attention in the paper of Yoshizawa (2002) on analysing the Direct Numerical Simulation backstep flow of LMK, bluff body (Obi and Nakatani, 2001) and trailing edge flows (Yao, Thomas, Sandham and Williams, 2001).

The study of LMK considered the boundary layer over a backstep, thus a flow which is initially uni-directional before separating at a discontinuity in the flow geometry. Interestingly when analysing the recirculating region downstream of the backstep they note similarities between the energy distribution found in the plane mixing layer, ie. a highly recirculatory flow.

In this work, the sheared cavity flow in both laminar and turbulent regimes, a fundamental wall bounded recirculating flow configuration, in addition to the non-bounded shearless turbulent mixing, are considered. Initially a comparative analysis of velocity and pressure fields for varying Reynolds number in the case of the cavity flows, and for varying energy ratio in the case of the turbulence mixing is presented. The energy budget is then observed in the mixing plane in these configurations, namely along the cavity mouth and in a plane at the

centre of the turbulent mixing layer, in order to further parameterize this re-distribution of energy. For the case of the cavity flows, where a mean flow is present, the mean as well as the fluctuating transports will be analysed in the cavity shear layer. It is not thought that a study based on the mean flow variables has previously been carried out, with Bailey, Abbà and Tordella (2008) the first to propose such a study.

In chapter 2 the physical problem is presented, where in section 2.1 the flow physics governing transport phenomena is discussed. Section 2.2 introduces the pressure-kinetic energy balance. The energy balance equation is derived from the kinetic energy transport equation, and previous findings from literature regarding the roles played by the pressure and kinetic transport in zones of recirculation are presented.

In chapter 3 the flow states considered in this study are introduced, with in section 3.1 the cavity flow, discussing first relevant studies already in literature in sub-section 3.1.1 and then the two numerical tools, their development and verification, used in this study. Two DNS codes have been employed to carryout the channel-cavity simulations, both finite difference implementations of the incompressible Navier Stokes equations. Further details of their development and implementation can be found in sub-sections 3.1.2-3.1.5. In sub-section 3.1.6 the characteristics of the flow are presented, culminating in profiles of the pressure, velocity and kinetic energy at the mouth of the cavity. In the final part of this chapter, sub-section 3.1.7, the turbulent cavity flow configuration is considered, together with the particulars relating to its more complex setup.

The following section 3.2 then moves on to the shearless mixing. In this section the shearless turbulent mixing of two decaying homogeneous isotropic turbulent (HIT) fields is presented, for mixings differing only due to their energy content. The development of turbulent intermittence from an initial Gaussian state, and the energy/pressure transport from initial zero values is presented through analysis of the velocity statistics. Since the flow is devoid of the production of turbulence kinetic energy, the study allows the study of the finer mechanisms involved in the energy balance. In sub-sections 3.2.1-2 the background and theory is presented, in 3.2.3 methodology and in the final part 3.2.4 the results of the simulations.

In chapter 4 the energy balance analysis is then carried out for all the flow configurations considered. Starting with the mean energy balance in the laminar and turbulent cavity flows in section 4.1. The fluctuating energy balance in for the cavity flows is then considered in section 4.2, and in the final section 4.3 for the shearless turbulent mixing.

In the final chapter concluding remarks and further developments and applications are given.

2. The Physical Problem

In chapter 2 the physical problem is presented. The phenomena of transport in fluids is discussed and several important aspects are considered: the Reynolds number of the flow, and transport at the molecular level. The chapter is split into two sections where section 2.1 the flow physics governing transport phenomena is discussed. In section 2.2 the pressure-kinetic energy balance equation is derived and previous findings regarding the importance of the terms in zones of recirculation is presented.

2.1. Transport

2.1.1 Introduction

Transport within a medium is a result of a non uniform distribution of the properties of the medium. Fluids tend to an equilibrium state where a balance is reached between the inertial and the molecular transport properties. In an inhomogeneous configuration, molecular level agitation causes the transport of species, momentum and internal energy (Batchelor, 1990) from regions of high concentration to those of lower concentration. Heat is conducted and momentum is exchanged through the action of viscosity.

In the continuous Navier Stokes equation (2.1), accompanied by the continuity equation (2.2), these transports are represented by the diffusion of momentum, factored by a molecular diffusion coefficient, and by the convection of momentum in the non-linear inertial term.

$$\frac{\partial \bar{u}}{\partial t} + \bar{u}.\nabla \bar{u} = -\frac{1}{\rho}\nabla p + \frac{\mu}{\rho}\Delta \bar{u} \ (2.1)$$

$$\frac{\partial \rho}{\partial t} + \nabla.(\rho \bar{u}) = 0 \ (2.2)$$

2.1.2 Significance of Reynolds Number

The ratio of inertia to viscous forces, the Reynolds number (2.3), , is a measure of the relative importance of the convection and diffusion terms in the Navier Stokes equation. For high Reynolds number flows, diffusion almost becomes insignificant, only remaining important in thin layers close to boundaries, or where large gradients of the flow properties of state can be found such as in shock waves, and at the dissipation scale of turbulence in the vortical filaments. Apart from these instances, the transport by the inertia of the flow, the

convection, is much greater than the effects of molecular transport, and the Navier Stokes becomes a balance of the pressure and convection terms.

$$\mathrm{Re} = \frac{\rho u d}{\mu} \quad (2.3)$$

In low Reynolds number flows the flow properties are more diffused owing to the greater molecular transport, in a Stokes flow the non-linear inertial term is insignificant and an be omitted from the momentum equation (2.4).

$$\frac{\partial \bar{u}}{\partial t} = -\frac{1}{\rho}\nabla p + \frac{\mu}{\rho}\Delta \bar{u} \quad (2.4)$$

For flows in which viscous effects are unimportant, ie. flows at high Reynolds number, or the flow at a large distance from a boundary, the inertia term dominates and the Euler equation (2.5) can be used.

$$\frac{\partial \bar{u}}{\partial t} + \bar{u}.\nabla \bar{u} = -\frac{1}{\rho}\nabla p \quad (2.5)$$

2.1.3 Implications of Molecular Level Transport (Shear)

When adjacent elements of a fluid moving at differing velocities mix, friction forces are set up as a result of the molecular level transport interactions. Groups of molecules from each of the elements diffuse into the neighbouring element and molecular attraction/repulsion forces act to dissipate energy, tending to smooth spatial variations of the velocity. For Newtonian fluids Stokes' hypothesis holds, in that viscous stresses are linearly related to the rate of strain of a fluid element.

Over the area of interaction surface between the two elements, this shear acts to dissipate kinetic energy, turning it to heat energy. Regions of shear may give rise to instability, here energy is taken from the mean velocity field, with turbulent kinetic energy produced. At high Reynolds numbers shear layers are a source of many vortical scales, turbulent kinetic energy and vorticity.

The flow close to a boundary is forced, by the condition of no-slip, to approach the velocity of its boundary, where there is no relative movement between the molecules of the

boundary and the molecules of the fluid. If the velocity of the boundary is different from that of the flow far from the boundaries, and often one of the media is stationary (eg. flow moving past a sphere, or a sphere moving through a fluid), then this sets up a volume where these molecular interactions dominate in the vicinity of the boundary. In this boundary layer the shearing effect is associated with flow momentum loss and a skin friction drag.

Separation of this boundary layer can occur when an adverse pressure gradient is present, in this situation the flow particles are losing kinetic energy. The particles closest to the boundary have the least kinetic energy, and it is possible that the fluid has zero velocity offset from the boundary. Downstream of separation point, in both laminar and turbulent flows, there exists a recirculation zone in which the flow closest to the boundary moves in the opposite sense to the freestream. This flow tends to be unsteady. An adverse pressure gradient can be caused by a diverging geometry, such as an expanding channel or the convex surface of an aerofoil, or a sudden expansion, such as downstream of a backstep or bluff body.

As shall be shown in the following chapters these regions of non-uniformity and shear bring about differing importance in the role played between terms in the energy balance of the flow.

2.2. Energy Balance

In the next section, working from the equations for energy as presented in Batchelor (1990), (eqn.s 3.3.1, 3.4.3, 3.5.1), the energy balance equation will be derived, focussing on the relations between the transport of kinetic energy, and on the transport of energy in the form of pressure.

2.2.1 Derivation of Energy Balance Equation

For a fluid moving with velocity $\vec{u}$, the rate of change of kinetic energy per unit mass is expressed

$$\frac{\partial \frac{u_i u_i}{2}}{\partial t} + \frac{\partial \frac{u_i u_i}{2} u_j}{\partial x_j} = -\frac{1}{\rho}\frac{\partial}{\partial x_j} p u_i \delta_{ij} + \frac{\mu}{\rho}\frac{\partial}{\partial x_j}\left[\left(\frac{\partial u_i}{\partial x_j} + \frac{\partial u_j}{\partial x_i}\right)u_i\right] - \frac{\mu}{\rho}\left(\frac{\partial u_i}{\partial x_j} + \frac{\partial u_j}{\partial x_i}\right)\frac{\partial}{\partial x_j}u_i$$

(2.6)

Where $\quad \frac{1}{2}\vec{u}^2 \quad$ is the kinetic energy of the bulk flow

e   the internal energy

10

$$F_i \qquad \text{a body force in direction i}$$

$$\rho \qquad \text{fluid density}$$

$$\sigma_{ij} \qquad \text{stress tensor}$$

$$\text{k} \qquad \text{thermal conductivity}$$

$$\text{T} \qquad \text{temperature}$$

$$\frac{\partial \frac{u_i u_i}{2}}{\partial t} + \frac{\partial \frac{u_i u_i}{2} u_j}{\partial x_j} = -\frac{1}{\rho}\frac{\partial}{\partial x_j} p u_i \delta_{ij} - \varepsilon + \kappa \quad (2.7)$$

Where
$$\eta = \frac{\mu}{\rho}\frac{\partial}{\partial x_j}\left[\left(\frac{\partial u_i}{\partial x_j} + \frac{\partial u_j}{\partial x_i}\right)u_i\right] \qquad \text{viscous diffusion}$$

$$\varepsilon = -\frac{\mu}{\rho}\left(\frac{\partial u_i}{\partial x_j} + \frac{\partial u_j}{\partial x_i}\right)\frac{\partial}{\partial x_j}u_i \qquad \text{dissipation}$$

$$\frac{\partial \frac{u_i u_i}{2}}{\partial t} + \frac{\partial \phi}{\partial x_j} = \varepsilon + \eta \quad (2.8)$$

Where
$$\phi_j = u_j E + \frac{1}{\rho}p u_j, \qquad E = \frac{u_i u_i}{2} \text{ kinetic energy per unit mass}$$

Introducing a coefficient α into the energy balance equation we can represent the pressure transport, $\overline{pv}$, as some factor of the kinetic energy transport $\rho v \overline{\dfrac{u_i u_i}{2}}$.

$$\overline{pv} = \alpha \rho v \overline{\frac{u_i u_i}{2}} \quad (2.9)$$

2.2.2 *Energy Balance in Recirculatory Turbulent Configurations*

In turbulent flows it is well known that the production and dissipation of turbulent kinetic energy reach peaks close to boundaries. The pressure and turbulent kinetic energy transport also increase close to walls. In general it scales with the convective transport, Yoshizawa (2002). Yoshizawa goes on to note that the combined sum of the pressure and kinetic energy transports are everywhere else in the channel, much less than the production and dissipation terms, albeit except for the centreline region where production and dissipation are relatively low.

The relative magnitude of the various terms can be seen in the profiles of the turbulent kinetic energy budget taken from LMK in figure 2.1. At 2 step heights upstream of a turbulent backstep flow the pressure and turbulent kinetic energy transport terms are relatively low compared to the production and viscous dissipation terms, except in the near wall region. At 4 step heights downstream of the backstep, thus in the recirculating region, the maximum value of the pressure transport doubles with respect to its upstream value, whereas the maximum turbulent kinetic energy transport almost halves. Note also a sign reversal for the coefficient α. Upstream of the backstep Pk and Tk are of the same sign near the wall, thus α is negative and the transports are in the same direction. Moving away from the wall Tk reverses sign, thus also α. In the recirculating region Pk and Tk are of opposite sign, thus α is negative.

Flows in which large convective transports can be found include those in which there are large changes in the streamwise direction, so in addition to backsteps one can include bluff bodies (Yao, Thomas, Sandham, Williams 2001) and cavity flows. It is in these flow configurations in which these two terms, the pressure and kinetic energy transports, become influential in the energy balance, and indeed the relative magnitudes of the two terms, and not just the sum, is now also of interest. Yoshizawa notes that pressure transport is generally considered to be 10% the value of the kinetic energy transport. As discussed above, when entering regions of high recirculation there is a redistribution of energy between these two terms, with the pressure transport taking on a greater role.
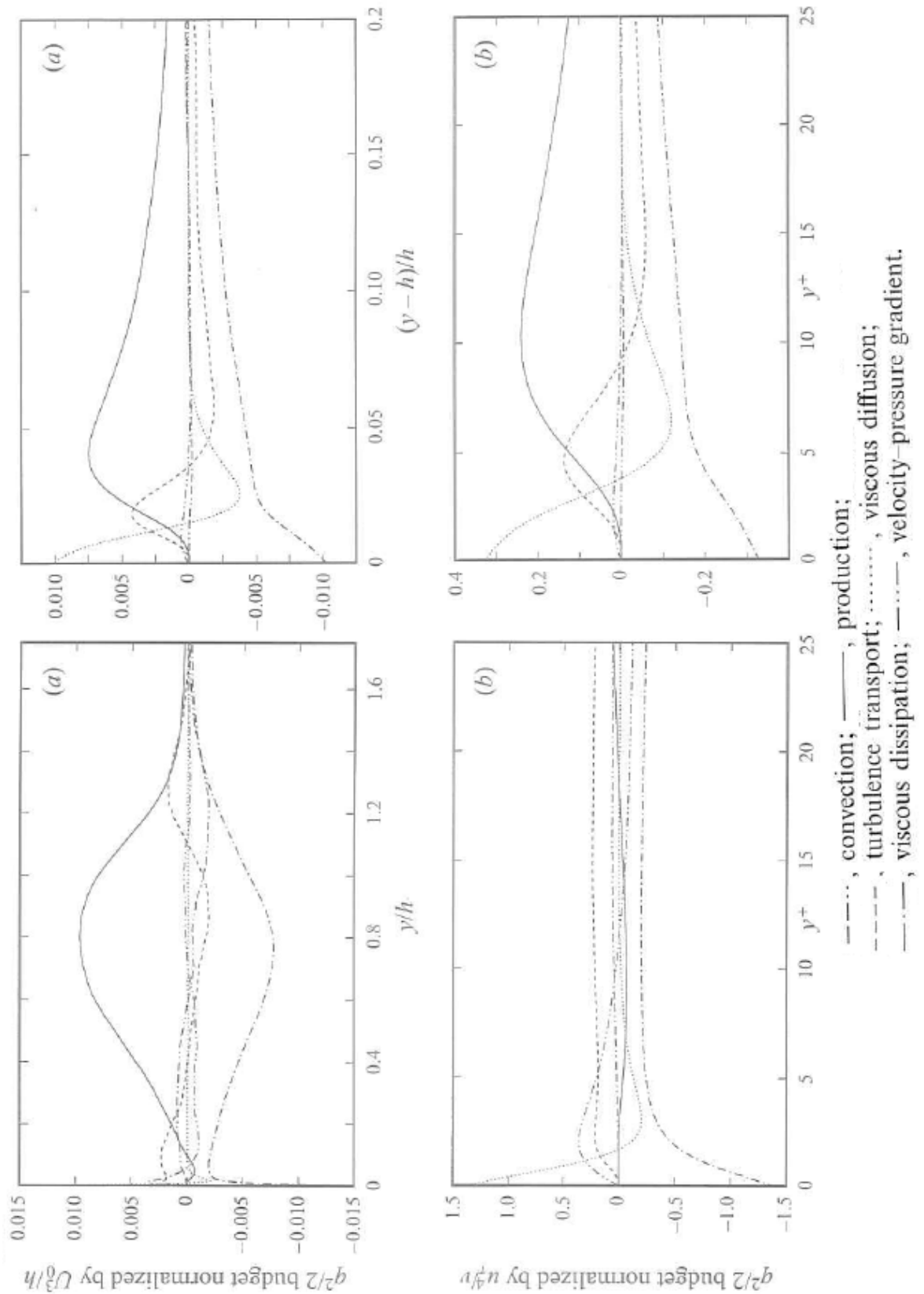
Figure 2.1. Kinetic energy budget in the backstep flow, taken from DNS simulation of Le, Moin and Kim (1997) (LMK). Top figure is at 2 step heights upstream of backstep, bottom figure is within recirculation zone 4 step heights downstream of backstep. a) Away from the wall, b) near the wall.

13

2.2.3 Mean and Fluctuating Components: Transports / Correlations

A number of differing terminologies are used in literature to refer to the various transport terms. For clarity in the second column of table 2.1 the relevant versions that will be referred to in this text are listed. Here the velocity/pressure can be mean or fluctuating values, depending on the context. Particularly, Yoshizawa (2002) often refers to the term $\rho u_j u_i u_i$ as a triple velocity correlation, and later in his paper drops the 'triple' to name this same term the 'velocity correlation'. Here this triple moment is given its full and non ambiguous title, the kinetic energy transport.

In turbulent flows the transport terms based on the fluctuating components are synonymous with correlations, usually the mean component is not considered in this context.

	Terms used in this work	Frequently synonyms found in literature	Type of transport
ρu_i	Mass transport		Scalar
$\rho u_i u_j$	Momentum transport	(co)Variance / Velocity correlation	Vector
$\rho u_j u_i u_i$	Kinetic energy transport	Triple velocity correlation	Scalar
$P u_i$	Pressure transport	Pressure-velocity correlation	Scalar

Table 2.1. Definitions of transport terms.

3. Flow States and Methodologies

In this chapter the two flow configurations considered in this study, the laminar and turbulent cavity flow and the homogeneous isotropic shearless turbulent mixing, are presented. The basic flow states are shown without at the stage determining the energy balance.

The first section 3.1 considers laminar and turbulent cavity flows in a channel. The velocity and pressure fields in the cavity, along the channel and at the mouth of the cavity are presented for flows over a range Reynolds numbers. In the first sub-section 3.1.1 the relevant studies already in literature are discussed, then in sections 3.1.2-5 the development and verification of the two numerical methods used in this study is presented. In the final two sub-sections the results of the cavity flow simulations are presented and compared with those found in literature, with in 3.1.6 the laminar results and in 3.1.7 the turbulent case. Further discussion of the methodology and proof of verification can be found in the turbulent sub-section owing to the added complexity of the method.

The following section 3.2 then moves on to the shearless turbulent mixing of two decaying homogeneous isotropic turbulent (HIT) fields, for mixings differing only due to their energy content. The development of turbulent intermittence from an initial Gaussian state, and the energy/pressure transport from initial zero values is presented through analysis of the velocity statistics. Since the flow is devoid of the production of turbulence kinetic energy, the study allows the study of the finer mechanisms involved in the energy balance. Sections 3.2.1 and 3.2.2 introduce the topic and the background, the numerical methodology employed is presented in section 3.2.3, and the results are presented in section 3.2.4.

3.1. Cavity Flows

3.1.1 Laminar, Transitional, Turbulent: Bibliography

The cavity problem presents two main phenomena: flow separation and vortex formation. Focusing only on rectangular geometries, the nature of this separated recirculating flow depends upon the Reynolds number, the upstream flow regime, as well as the cavity aspect ratio.

In internal flow applications, such as channels or turbines, the flow is almost always turbulent. Discontinuities or expansions in geometry cause the flow to lose kinetic energy and

make it susceptible to reverse in direction in the vicinity of boundaries, this gives rise to recirculation zones, greater shear and thus greater instability. In these flow situations a greater energy is required to overcome drag and maintain the required flow rate. One key example is the highly tuned flow within a turbine. Since turbines are responsible for providing are large proportion of global energy consumption, a small improvement in the flow efficiency can have great effects both fiscally and environmentally.

Despite the fact that most flows in both engineering and in nature are turbulent, the laminar cavity flow is still of significant importance. Indeed Krishnamurty (1956) found that laminar upstream boundary layers gave rise to higher sound pressure levels (SPL) than the corresponding turbulent flow, and Howe (1997) showed not only that laminar mean flows can induce oscillations, but that laminar flow resonances are often more intense. A laminar flow regime is not only an interesting point, but also and important point from which to consider a wide range of Reynolds numbers for a complete study of the dynamics of a flow configuration.

The engineering interest in the area of cavity flows is primarily motivated by the requirement to reduce the noise impact of commercial aircraft. A large fraction of this noise is derived from the jet engines, however due to major advances in this field over the past decade, fuselage induced noise is now an equally contributing factor, Morris (2007). Relevant geometrical features of the fuselage include window gaskets, discontinuities over wings and flaps, fuel vents, and wheel wells, Camussi, Guj and Ragni (2006). Air frame noise mainly generated by the flow control devices and the lowered undercarriage reaches a peak on final approach to landing, this phase of flight is coincident with the closest vicinity to large urban areas. Also of concern is the vibrational loading induced by the oscillating flow, a potential source of fatigue, component damage and passenger discomfort, as well as an increased skin friction and form drag, which reduce the aerodynamic performance and create a greater environmental impact.

Further settings in which cavity flows are of significant importance are in the cooling towers of computers, the aerodynamics of road vehicles and trains, as well as sound/pressure wave absorption devices where a ridges present an increased surface area compared to a flat profile. More recently, with the development of commercial aircraft with greater payloads and range, cavities are used as a means of flow control on the upper side of low aspect ratio wings, increasing boundary layer vorticity to suppress separation.

In both laminar and turbulent cavity flows, after separation at the upstream edge, the mean flow forms a vortex of the dimension of the cavity depth. Reattachment to the floor of the

cavity depends on its aspect ratio. For a laminar cavity reattachment is dependent on Re and is typically of the order 10 cavity depths downstream of the upstream edge. For a turbulent cavity this is less dependent on the Re and is widely accepted to be around 6 cavity depths downstream of upstream edge, Sinha, Gupta and Oberai (1982). The region between this reattachment point and the upstream edge is dominated by a large recirculation. For flows with cavity aspect ratios less than these values, except for Stokes flows at low Re, the cavity is likely to be 'open', in which after separating from the leading edge reattachment takes place downstream of the trailing edge. The whole cavity is then dominated by a recirculation region with, for higher Re, the principal eddy located close to the downstream edge. For cavity flows where reattachment takes place on the cavity floor, the cavity is termed 'closed'. Here, beyond the upstream recirculation zone there exists a region of uni-directional flow parallel to the cavity floor until the flow re-separates close to the downstream edge, and a second recirculation region is here present.

A rectangular cavity having aspect ratio greater than 1 is termed shallow, otherwise deep after Sarohia (1977).

Although the rectangular cavity represents a basic geometrical form, it has been studied in various simpler forms, allowing the researcher to concentrate on the vortex formation, transitions and instabilities. The lid driven cavity, that is an enclosure in which one or more of the boundaries drives the flow, has been studied analytically, numerically and experimentally. The review of Shankar and Deshpande (2000) summarizes this history. In this context the flow is driven by the movement of one or more of the bounding walls and not through the shear of a flow external to the cavity. A square cavity is by far the most frequently studied geometry. Theofilis, Duck and Owen (2003), is an example of such work, studying the instability of flow in four enclosed flow configurations, working from a plane channel, to the 2D version of the laminar Poiseuille pipe flow, through to the 2D counterpart to Couette flows, before considering the lid-driven cavity.

The structure of turbulent boundary layer over rectangular roughness, ie. 2D cavities, has been studied in water tunnel experiments (Djenidi, Elavarasan & Antonia 1999) and also in the DNS of a turbulent channel cavity flow at Re_tau=180 by members of the same group (Leonardi, Orlandi, Smalley, Djenidi & Antonia 2003, Leonardi, Orlandi, Djenidi & Antonia 2004). In the numerical studies recirculation and reattachment has been considered for various cavity aspect ratios for $0.33 < D < 39$, analyzing the drag, Reynolds stress distributions and velocity profiles, as well as the roughness/cavity interaction with the structure of the turbulent boundary layer. For aspect ratios lower than 7 the flow, after separating at the upstream edge,

reattaches downstream of the opposite edge, for greater aspect ratios the cavity is closed. The numerical domain is however periodic in the streamwise direction, thus given that the configuration is an infinitely long rough wall channel all the cavities have disturbed upstream turbulent boundary layers.

Oscillations in cavity flows can be caused by a number of interacting acoustic and fluid dynamics phenomena. A recent overview of the studies into understanding these phenomena and developments towards controlling oscillating cavity flows is given by Rowley and Williams (Ann. Rev. 2000). An important point made by these authors is that the aim of controlling this flow is not particularly to avoid the oscillations, but to reduce the amplitude of the tones.

When considering numerical approaches to the study of the aero-acoustics of cavity flows it is very rare to find studies of both the fluid dynamics of the cavity (the acoustic source region) and the far field noise propagation, without the use of a model for one of the two regions. The fine resolution required in the cavity and the long domain needed to model pressure wave propagation make this an expensive task, De Roeck, Desmet, Baelmans and Sas (2004), and hybrid methods are commonly preferred, Terracol, Manoha, Herrero, Labourasse, Redonnet, Sagaut (2005).

In this study the boundary layer thickness over cavity depth ratio is low, thus the acoustic feedback mechanisms, see Rowley and Williams (2006) are secondary. This work will therefore concentrate on the fluid dynamics dominated cavity flow more than acoustic effects. The Reynolds number is defined by the parameters driving the flow, thus the channel bulk velocity and the channel half height. This relation will be denoted Re from now on.

3.1.2 Methodology: DNS Code, Fractional Step Method

The incompressible non-dimensional Navier Stokes equations in conservative form (3.1) are solved using a fractional step method, of the type Moin & Kim (1985). The scheme is second order finite difference, with velocities and pressure collocated in a staggered arrangement, see scheme in figure 3.1.

$$\frac{\partial \bar{u}}{\partial t} + \nabla(\bar{u}.\bar{u}) = -\nabla p + \frac{1}{\text{Re}}\Delta(\bar{u}) \quad (3.1)$$

In the fractional step method the momentum equations are solved first without the presence of pressure, see the sequence in equations (3.2-8). Pressure is subsequently included in the

equations on enforcing a divergence free velocity field, where its solution is reduced to the solution of the Poisson equation. The scheme employs fourth order Runge Kutta time integration, in which pressure is calculated on each sub step.

$$\frac{\overline{u}^{n+1} - \overline{u}^n}{\Delta t} = \frac{1}{\text{Re}} \nabla^2 \overline{u} - \nabla.(\overline{u}.\overline{u}) - \nabla p \quad (3.2)$$

$$\frac{\overline{u}^* - \overline{u}^n}{\Delta t} = \frac{1}{\text{Re}} \nabla^2 \overline{u} - \nabla.(\overline{u}.\overline{u}) \quad (3.3)$$

$$\overline{u}^* = \overline{u}^n + \Delta t \left[\frac{1}{\text{Re}} \nabla^2 \overline{u} - \nabla.(\overline{u}.\overline{u}) \right] \quad (3.4)$$

$$\overline{u}^{n+1} = \overline{u}^* - \nabla p \Delta t \quad (3.5)$$

$$\nabla^2 P = \frac{\nabla.\overline{u}^*}{\Delta t} - \frac{\nabla.\overline{u}^{n+1}}{\Delta t} \quad (3.6)$$

$$\nabla.\overline{u}^{n+1} = \nabla.\overline{u}^n = 0 \quad (3.7)$$

$$\nabla^2 P = \frac{\nabla.\overline{u}^*}{\Delta t} \quad (3.8)$$

The convection and diffusion terms are solved in 3D by second order finite differencing, whereas the laplacian for pressure is discretised in independent 2D x-y planes. A direct method, employing a matrix inversion technique, UmfPack, Davis and Duff (1997), is used to give a solution to the relation Ax=b, where A is an n-by-n sparse linear matrix, and x and b are n dimensional vectors. In the remaining periodic z-direction a Fourier-Galerkin method is used for the solution of pressure. The revised solution for the Poisson equation is shown in equation 3.9.

$$\frac{\partial^2 P}{\partial x^2} + \frac{\partial^2 P}{\partial y^2} - k_z^2 P = \frac{\nabla.u^*}{\Delta t} \quad (3.9)$$
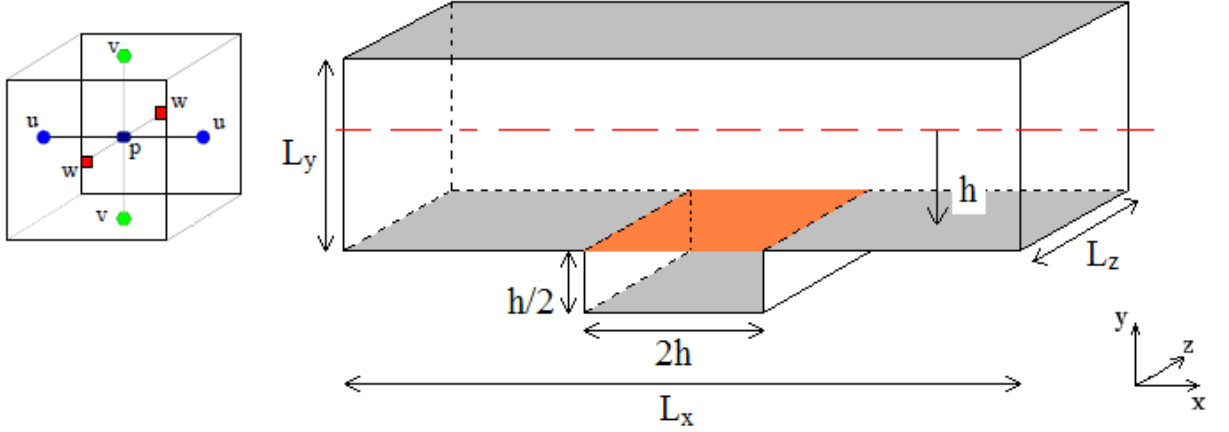
Figure 3.1. Scheme of the staggered grid arrangement, and the default domain coded into the Turin-DNS code.

The immersed boundary technique of Fadlun (2000) is employed to include the presence of the cavity in the flow domain, in which body surfaces can be imposed not necessarily coinciding with the computational grid, see schemes in figure 3.2. The method was initially developed by Peskin (1972) for application to internal blood vessel flows, and re-presented later by the same author, Peskin (2002). At the location of the body the no slip condition is applied to the velocity field, with wall boundary conditions also imposed for pressure. Note that the wall does not have to be stationary, and indeed could change form on each step or sub step.. A linear interpolation is deemed suitable for both laminar and turbulent flows to the nearest grid points within the flow. In the Turin code the immersed boundary technique is imposed at the same time as boundary conditions. An review of the immersed boundary technique can be found in Mittal and Iaccarino (2005).

To apply the immersed boundary technique a body force is added to the Navier Stokes equations (2.1). Within the body this force nullifies the velocity field, and for the flow far from the boundary the body force is zero. For the first computational points next to the boundary the force is applied so as to impose the no-slip condition at the location of the boundary – whether the boundary coincides with the grid mesh or not.

$$\frac{\partial \bar{u}}{\partial t} + \nabla(\bar{u}.\bar{u}) = -\nabla p + \frac{1}{\text{Re}} \Delta(\bar{u}) + f \quad (3.10)$$
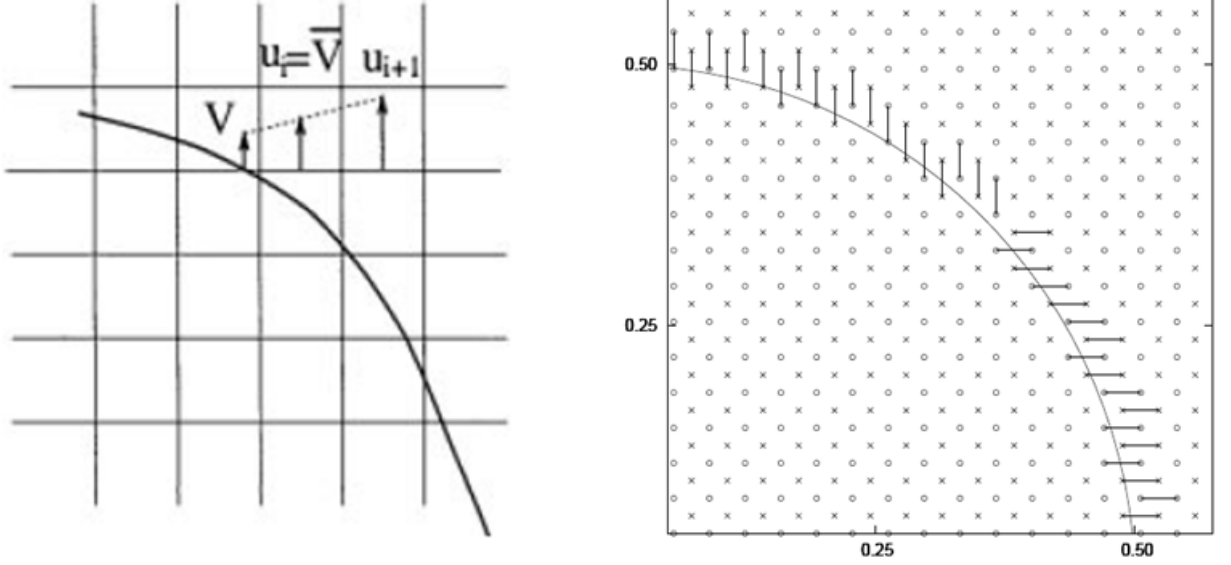
Figure 3.2. Implementation of the immersed boundary method, left scheme of Fadlun, Verzicco, Orlandi and Mohd-Yusof (2000) where the boundary velocity is interpolated to the nearest grid points, right, conventional interpolation direction from Giannetti and Luchini (2007), where interpolation is orthogonal to boundary surface.

3.1.3 Methodology: DNS Code, Mimetic Method of Abbà and Bonaventura

The second numerical tool used in this study is a mimetic implementation of the Navier Stokes equations. In this finite difference approach the Navier Stokes equations (2.1) have been reformulated using the identities of equations (3.11-12) to give the implemented equations (3.13-14). Mass and vorticity conservation are ensured through the discretisation of the relations, see Abbà & Bonaventura (2008) for further details and proof, and for the numerical validation of the scheme.

$$\vec{u}.\nabla\vec{u} = \omega\times\vec{u} + \nabla K \quad (3.11)$$

$$\Delta\vec{u} = \nabla(\nabla.\vec{u}) - \nabla\times\omega \quad (3.12)$$

$$\frac{\partial\vec{u}}{\partial t} = -\omega\times\vec{u} - \nabla(p + K) - \mu\nabla\times\omega \quad (3.13)$$

$$\nabla.(\vec{u}) = 0 \quad (3.14)$$

21

This method also uses a stepping method as presented in the previous section with the solution of pressure through the Poisson equation also solved using UmfPack. It also has an implementation of the immersed boundary technique, but here is more complex due to the introduction of the new variables. The immersed boundary technique must here be applied to the vorticity, kinetic energy and pressure fields.

3.1.4 Parallelisation of the Numerical Methods

The most time consuming and greatest memory requirement of the code is for the solution of the Poisson equation for pressure. In the scalar versions of the DNS codes this operation accounts for approximately 80% of the total cpu time requirement. In both DNS codes this aspect has been parallelized, with versions in OpenMP (shared memory directives) and mpi (message passing interface, distributed memeory directives) for the 'Turin DNS' method, and in mpi for the Mimetic method.

In the Mimetic method the memory requirements for the pressure routine has been completely distributed. This signifies that several variables, eg. $\nabla.\bar{u}^*$, never appear in a complete form on any one processor. This allows greater scalability of the code, since as the problem size increases, more processors can be used to distribute the problem over more memory.

The memory distribution of $\nabla.\bar{u}^*$ is represented in figure 3.3 for four processors. This term is the right hand side of the Poisson equation for pressure, which makes the sparse linear system. The domain is split in the x-direction, with each processor receiving $\nabla.\bar{u}^*$ for its part of the domain. The first operation to be performed on this variable is a conversion to Fourier space, which is then done in independent z-axes. Subsequently however, the linear system solves the Poisson equation in x-y planes, thus a redistribution of data is required since data in the x-direction is currently distributed. A data swap takes place with a tight condition that the whole variable does not appear on any one processor. At the end of the process the steps are reversed, with an inverse FFT in the z-direction giving the full solution for pressure. Using four processors the solution for the Poisson equation now accounts for approximately 50% of the total cpu time requirement.
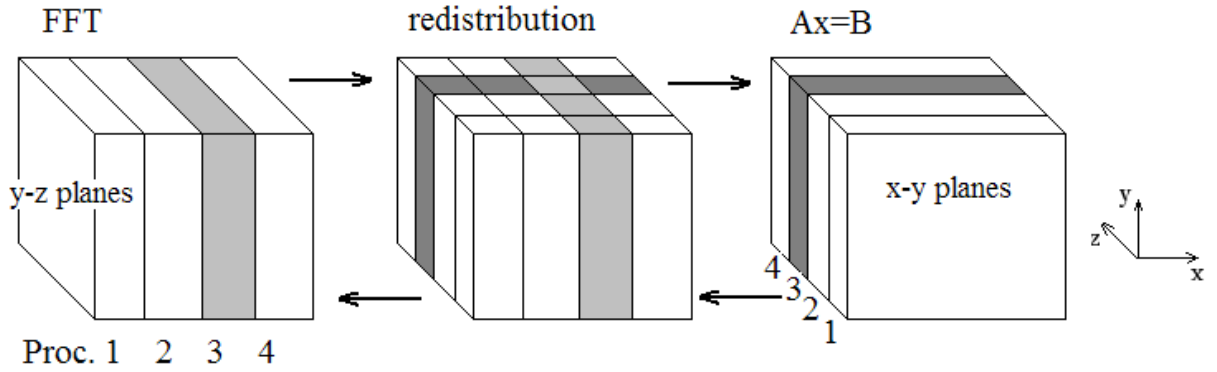
Figure 3.3. MPI distribution of $\nabla.\bar{u}^*$ for the FFT and sparse linear matrix methods.

3.1.5 Validation: Poiseuille and Backstep Flow in a Channel

Poiseuille

During the development stage of the 'Turin DNS' code, the initial test case was chosen to be the solution of Poiseuille's flow in a channel. The Poiseuille channel flow has a parabolic profile, and for a fully developed steady two dimensional flow since the flow is equal in every cross-section the convection term of the Navier Stokes equation is zero. The same is true for the diffusion terms in the streamwise and cross-stream direction with the result that the pressure gradient is balanced only by the diffusion term in the wall normal direction (equation 3.15), see Tritton (1984, eqn.s 2.1 – 2.6).

$$-\frac{dp}{dx} = \frac{d^2u}{dy^2} \quad (3.15)$$

Backstep flow of Armaly and Durst

A common source of verification for codes and models is the backstep problem, since it includes flow separation and reattachment points, and recirculation zones. The backstep experiment in an expanding channel of Armaly, Durst, Pereira and Schönung (1983) has been chosen to check the code since it includes more than one set of separation and reattachment points.

A Poiseuille flow with parabolic profile enters at the inlet. A very large expansion of the channel (2:3.88) then follows. For laminar flows the first reattachment length is greater than 10 step heights downstream of the edge. In this vicinity, owing to the large expansion ratio, the flow separates on the upper wall, thus forming a second zone of recirculating flow, smaller than the first and typically less than 10 step heights in length.
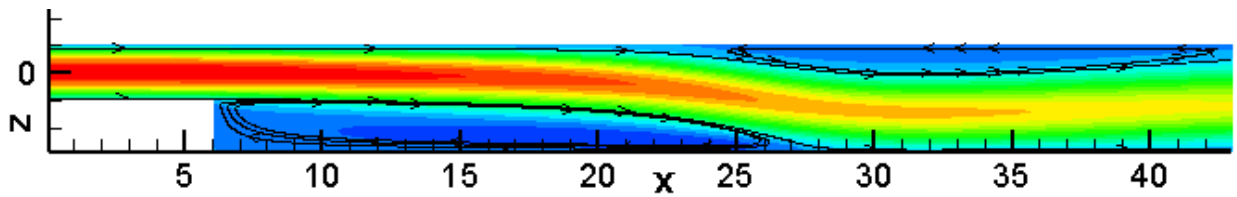
23

Figure 3.4. Streamlines of (u,v) and contours of streamwise u velocity for the DNS backstep flow.

For an inlet flow of Re_h=200 (corresponding to Re_D=800 for Armaly, Durst, Pereira and Schönung (1983), where the Reynolds number is defined with the hydraulic channel height), downstream of the backstep there should be, at approximately the same length as the reattachment on the lower wall (x1), a point of separation on the upper channel wall (x2), before its reattachement (x3), see the results in table 3.1 and streamline and contour plot in figure 3.4.

	x1	x2	x3
Armaly	14	11.5	20
Turin DNS	12.5	9.7	20.2

Table 3.1. Separation and reattachment lengths for the lab experiment of Armaly, Durst, Pereira and Schönung (1983), and the Turin DNS code.Length/step height.

Although there is not a complete agreement with the separation and reattachment lengths, there were several differences between the two experiments. The spanwise boundary conditions for the numerical case are periodic, thus a channel of infinite width, the results of Armaly are from the centre of a laboratory channel, thus in a bounded domain and considering only one 2D profile. The numerical mesh in the downstream portion of the channel has a streamwise spacing of the size 0.11 times the step height, a finer mesh is required to capture an accurate separation/reattachment point, but given the total length of the problem the number of computational points is already high. However, the ratios between the points are consistent. Chiang and Sheu (1999) noted differences with their numerical results were more pronounced on increasing the domain width, this fact supports these results since periodic spanwise conditions were used.

3.1.6 Results: Laminar Channel Cavity Flow

The computational domain considered is that of a channel with a cavity on the lower wall, as depicted in figure 3.1, of half height h, spanwise dimension π, and total length L=2π. The cavity is rectangular and is of constant aspect ratio 4 with length l=2h, and depth h/2. Also depicted in figure 3.1 is the cavity mouth, the interaction/shear plane between the cavity and the channel flow, profiles of the flow properties will be considered across this area. Note that using the coordinate system defined here a negative v velocity would be from the channel centre towards the cavity floor, thus into the cavity.

The initial condition in the channel is that of a fully developed laminar flow, ie. a parabolic profile as in the Poiseuille channel flow solutions of section 3.1.5. The initial flow velocity in the cavity is set to zero, and since the parabolic profile approaches zero at the channel wall there is no discontinuity in the initial velocity field at the cavity mouth. Integral and point values of the flow state in the cavity are used to determine the convergence of the solution, a typical temporal plot is shown in figure 3.5, for Re=1000. Note from this plot that the flow has been given an excessive number of iterations in order to allow any instabilities to develop, it does however develop to a steady flow solution.
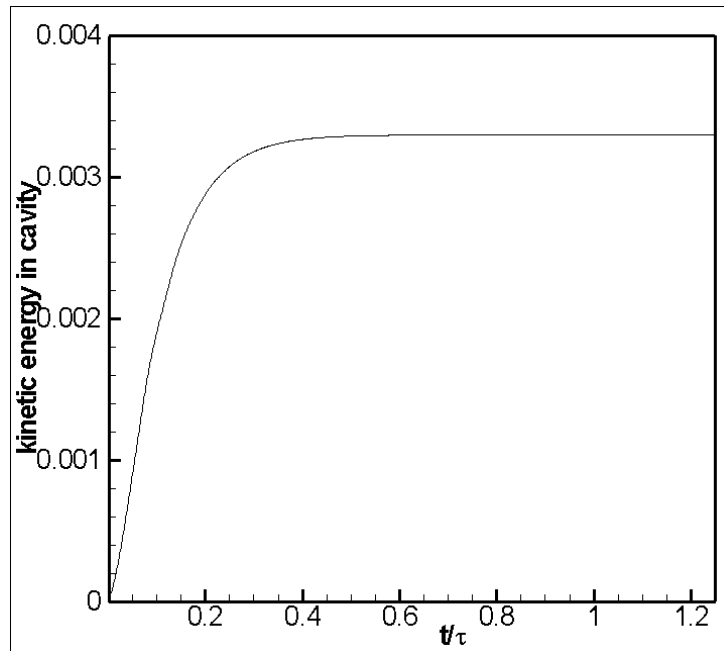
Figure 3.5. Convergence to a steady state of the total kinetic energy in the cavity for the case Re=1000, note that ample time was given for the development of any instability.

Reynolds numbers in the range Re $\in$ [50,2000] were considered, thus close to the Stokes regime, up to a limit for laminar flows in a channel. Table 3.2 lists dimensioned parameters based on the following flow conditions:

air at 20 °C and 1 bar,

dynamic viscosity $\mu=1.82 \times 10^{-5}$ Nsm^{-2},

density $\rho=1.19$ kgm^{-3},

channel half height=0.1 m.

When dealing with the dimensioned pressure, an ambient pressure of 1 atmosphere, 101250 Pa has been taken at the channel inlet.

L_x	h	L_z	U_{bulk}	Re	G
(m)	(m)	(m)	(m/s)		(mPa/m)
1,257	0,10	0,314	0,0038	25	-0,020865
1,257	0,10	0,314	0,0076	50	-0,041730
1,257	0,10	0,314	0,0153	100	-0,083461
1,257	0,10	0,314	0,0229	150	-0,125191
1,257	0,10	0,314	0,0306	200	-0,166922
1,257	0,10	0,314	0,0382	250	-0,208652
1,257	0,10	0,314	0,0459	300	-0,250383
1,257	0,10	0,314	0,0612	400	-0,333844
1,257	0,10	0,314	0,0765	500	-0,417305
1,257	0,10	0,314	0,1223	800	-0,667687
1,257	0,10	0,314	0,1529	1000	-0,834609
1,257	0,10	0,314	0,1835	1200	-1,001531
1,257	0,10	0,314	0,2294	1500	-1,251914
1,257	0,10	0,314	0,3058	2000	-1,669218
1,257	0,10	0,314	0,4434	2900	-9,826689
1,257	0,10	0,314	1,6819	11000	-77,423917

The mass flow for a fully developed Poiseuille channel flow, per unit time and per unit distance in the spanwise direction is given by: $U_{mass} = \dfrac{2G\rho h^3}{3\mu}$ Tritton (1984 [eqn 2.9]), where G is the pressure gradient per unit length.

From this relation we ascertain the bulk flow velocity, $U_{bulk} = \dfrac{Gh^2}{3\mu}$ since:

U_{mass} = fluid density . bulk flow velocity . total channel height $= \rho \dfrac{Gh^2}{3\mu} 2h$

Now defining the Reynolds number with the bulk velocity and the channel half height:

$Re = \dfrac{Gh^2}{3\mu}\dfrac{h\rho}{\mu} = \dfrac{Gh^3\rho}{3\mu^2}$

And rearranging to express the pressure gradient per unit length: $G = \dfrac{3\,Re\,\mu^2}{h^3\rho}$

Table 3.2. Dimensioned parameters for the laminar channel flows 50<Re<2000, and turbulent channel flows Re=2900 and Re=11000.

Figure 3.6 shows the dimensioned streamwise pressure distribution in the channel and cavity for four Re. The profiles are taken along the bottom wall of the channel and thus also along the cavity mouth, the location of the cavity is shown in the diagram. It can be seen that as Re is increased, and when considering a given fixed flow geometry, the pressure gradient required to overcome losses at the channel wall is greater for a greater velocity or a reduced fluid viscosity.

In the region of the cavity upstream edge the pressure drops suddenly and then increases downstream of the separation point. Moving downstream the channel pressure gradient is perturbed by the flow structures within the cavity, more evidently for the cases Re=1000 and Re=2000 where a dip in the profile can be noted close to the downstream edge. At the downstream edge there is a sharp peak in the profile at the point where the flow stagnates.
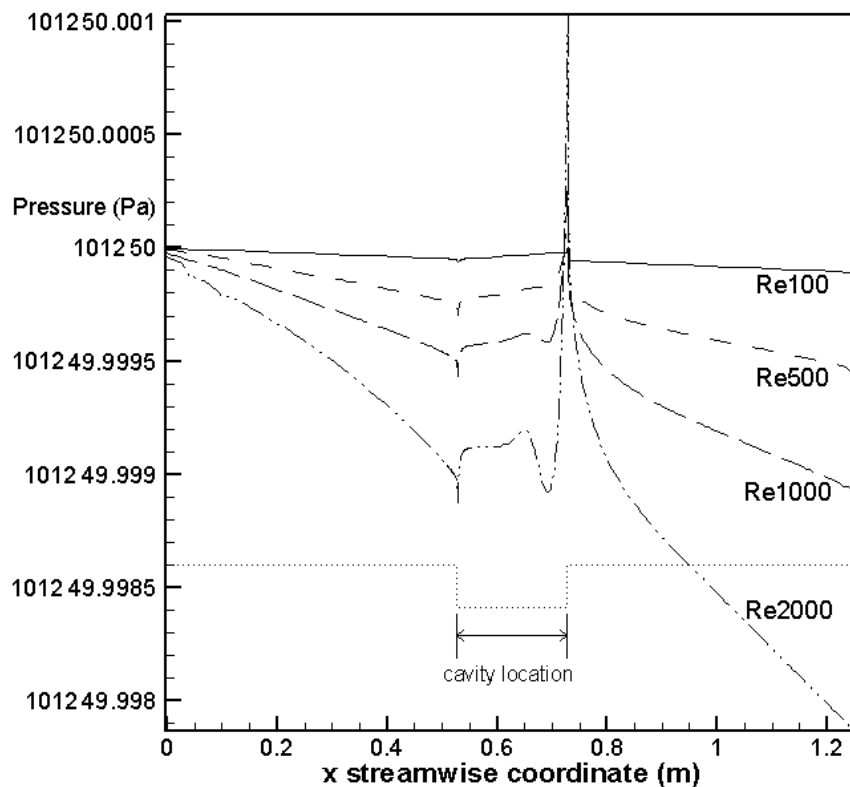
Figure 3.6. Dimensioned streamwise pressure profiles for Re=100, 500, 1000 and 2000, from the Mimetic code.

Now concentrating on a single Re, streamwise pressure profiles at various heights in the channel and cavity, for Re=1000, are plotted along with the analytical Poiseuille channel pressure profile in figure 3.7. It can be seen that the computational domain was of sufficient length to reconstruct the channel flow upstream and downstream of the cavity, since the

gradient matches that of the analytical result, with a perturbation caused in the region of the cavity, and no interference at the boundaries of the domain.
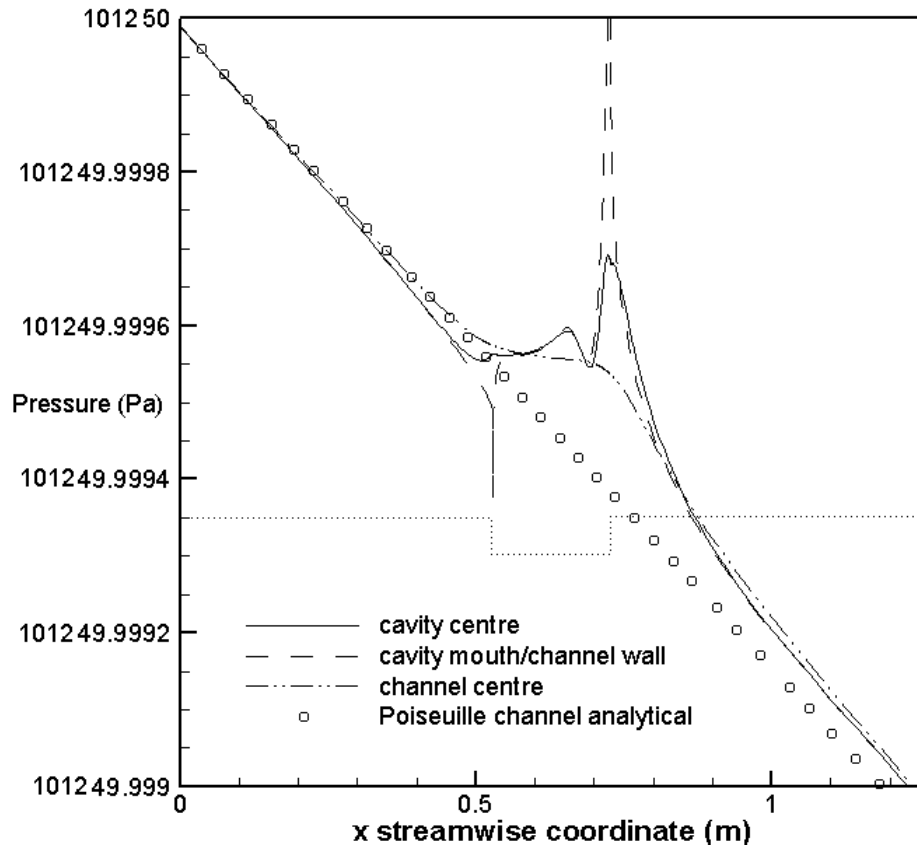

Figure 3.7. Streamwise pressure profiles at various heights in the channel and cavity for Re=1000, from the Turin DNS code.

The Re range considered is seen to give laminar-steady flows using both the Turin-DNS and Mimetic methods. Streamlines for this Re range can be seen in figure 3.8, and are followed by similar plots taken from literature, figure 3.9. Note that although one of the streamline plots from Grace, Dewar and Wroblewski (2004) has a laminar upstream boundary layer, the flow transitions to turbulent before reaching the cavity downstream edge.

It can be seen that for the lowest Re considered that the cavity flow is almost 'closed', ie. the flow almost reattaches to the floor of the cavity. On increasing Re, the principal eddy (PE), the dominant vortical motion in the cavity, moves from the vicinity of the upstream edge to close to the downstream edge. The location of the centre of the PE is plotted separately in figure 3.10, showing the movement downstream and deeper position into the cavity with increasing Re.

29
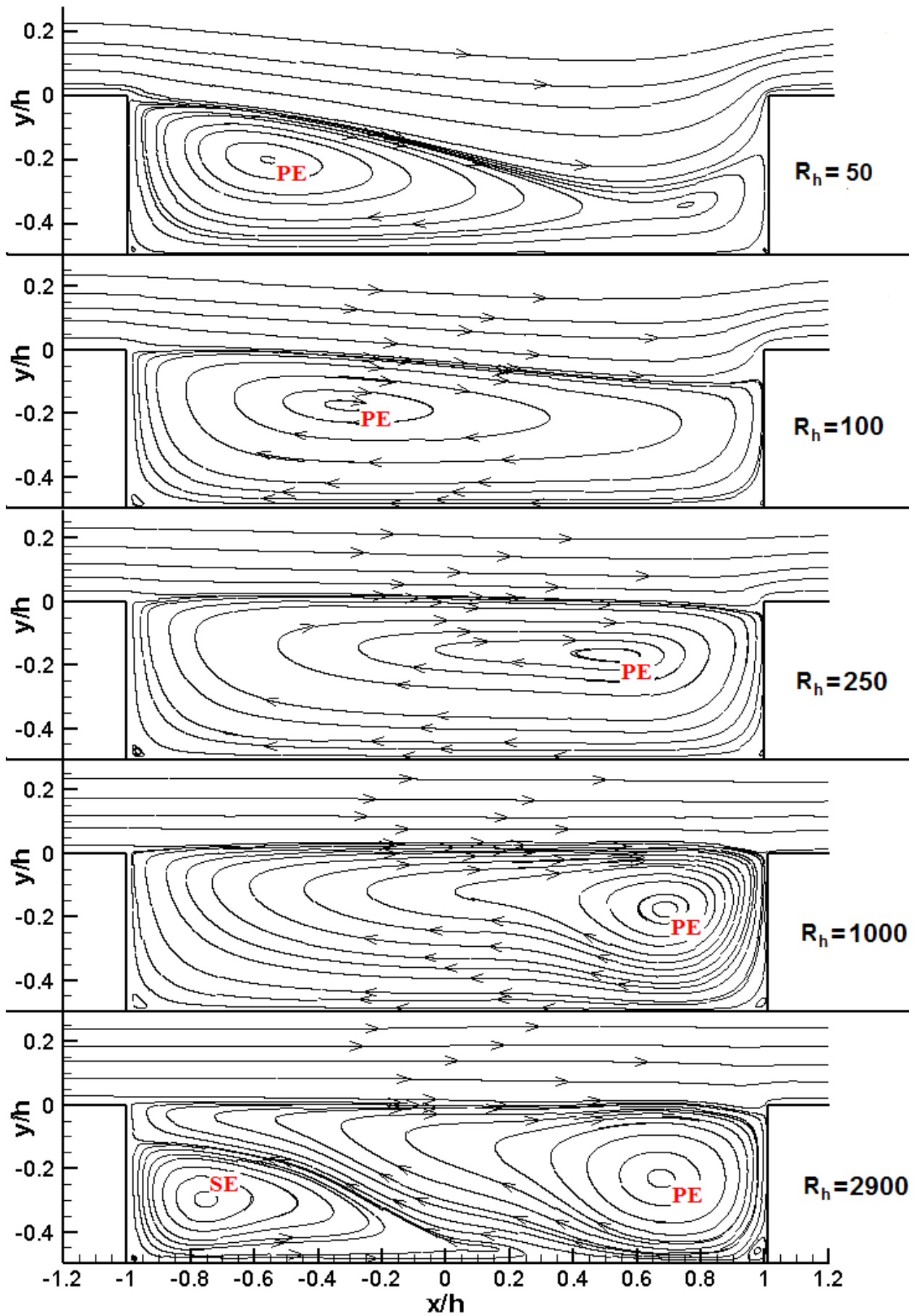
Figures 3.8. Streamlines (u,v) for the range of laminar and turbulent Re considered.

30
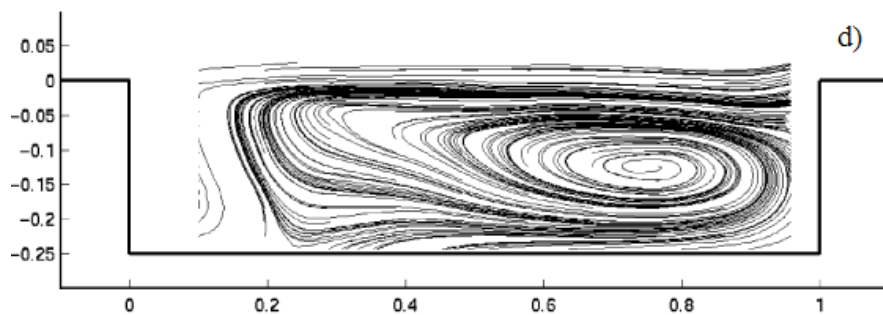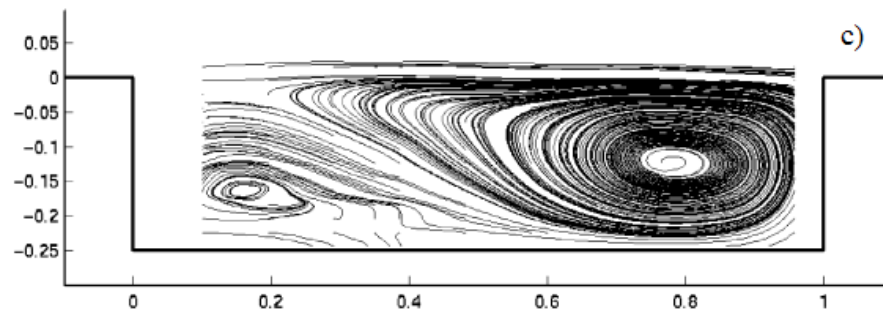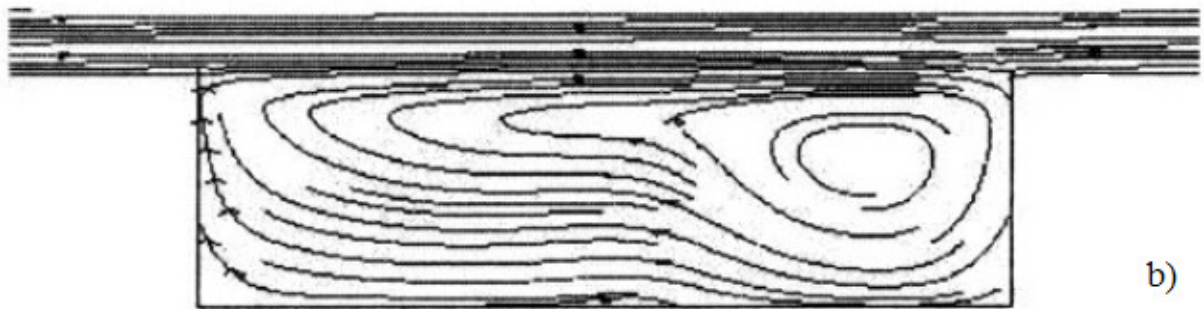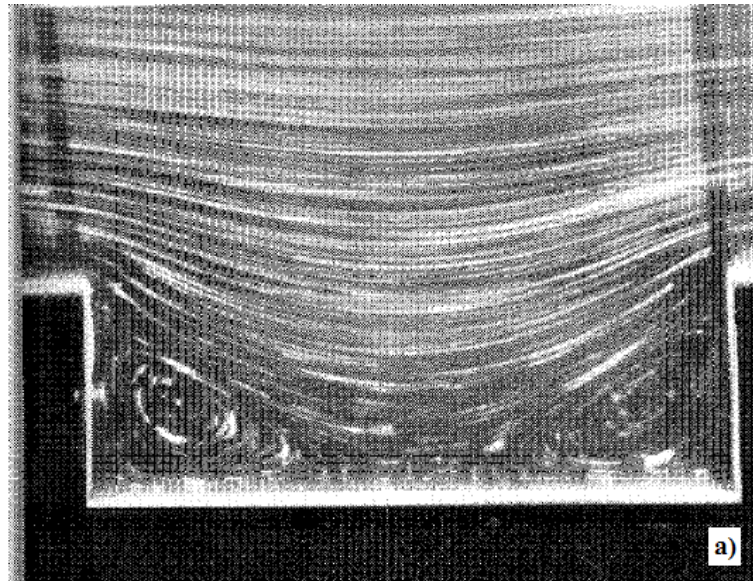
Figures 3.9. Streamline plots . a) low Re for a cavity of aspect ratio 3, the working fluid used was glycerine, Taneda (1979).b) numerical result from Yao, Cooper and Raghunathan. c) Wind tunnel flow with laminar upstream conditions and d) with turbulent upstream conditions from Grace, Dewar and Wroblewski (2004).
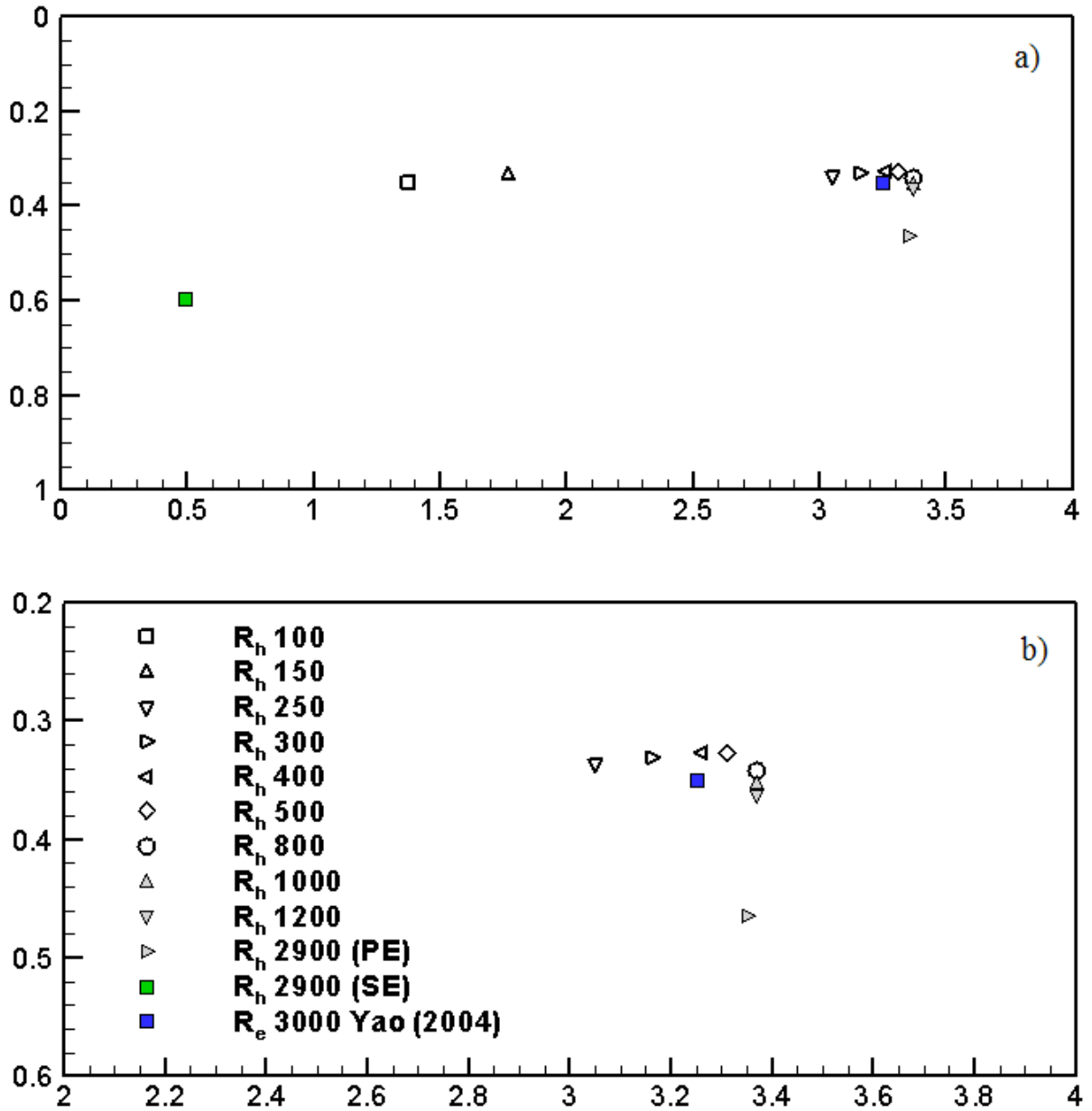
31

Figure 3.10. Location of the centre of the principal eddy within the cavity. a) full cavity, with one datum from Yao, Cooper and Raghunathan (2004) boundary layer experiemens, and the secondary eddy annotated for the Reh=2900 turbulent case. b) enlarged view of a downstream section of the cavity.

Now observing the flow properties at the cavity mouth it can be seen from the profiles of wall normal v-velocity in figure 3.11, that there tends to be a large area of low magnitude flow, followed by a confined region with a higher magnitude. For the laminar cases 500<Re<2000 this large area is an outflow, whereas for the turbulent case the flow direction and magnitude oscilates, with a peak inflow flanked by two areas of outflow. For all these Re there than follows a high magnitude inflow into the cavity in the vicinity of the downstream

edge. In the case of Re=100, which corresponds to partially open case, the behaviour is different however. An outflow exists close to both the edges, with a large area of low velocity inflow between them.

The total velocity entering and exiting the cavity must be zero in this incompressible flow. From the velocity plot it can be seen that the momentum exchange, ie. the magnitude of the total momentum flux in the positive wall normal directions, and the negative wall normal direction, is linearly proportional to Re. The momentum exchange has been plotted in figure 3.12 with a fitting showing that it is directly proportional to Re.
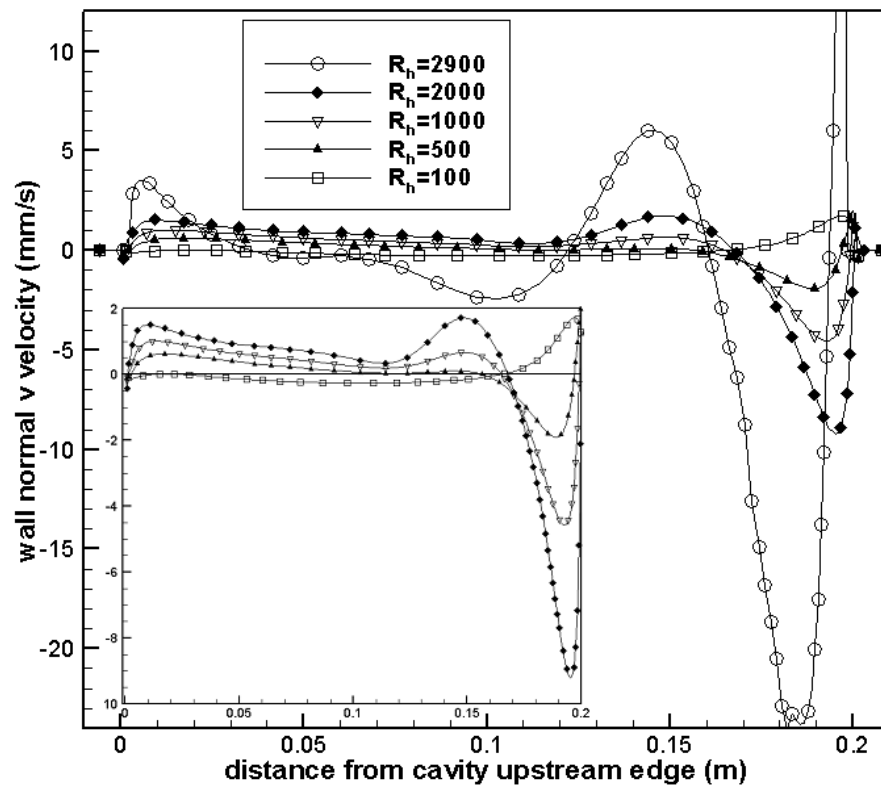
Figure 3.11. Dimensioned v wall normal velocity across the mouth of the cavity.
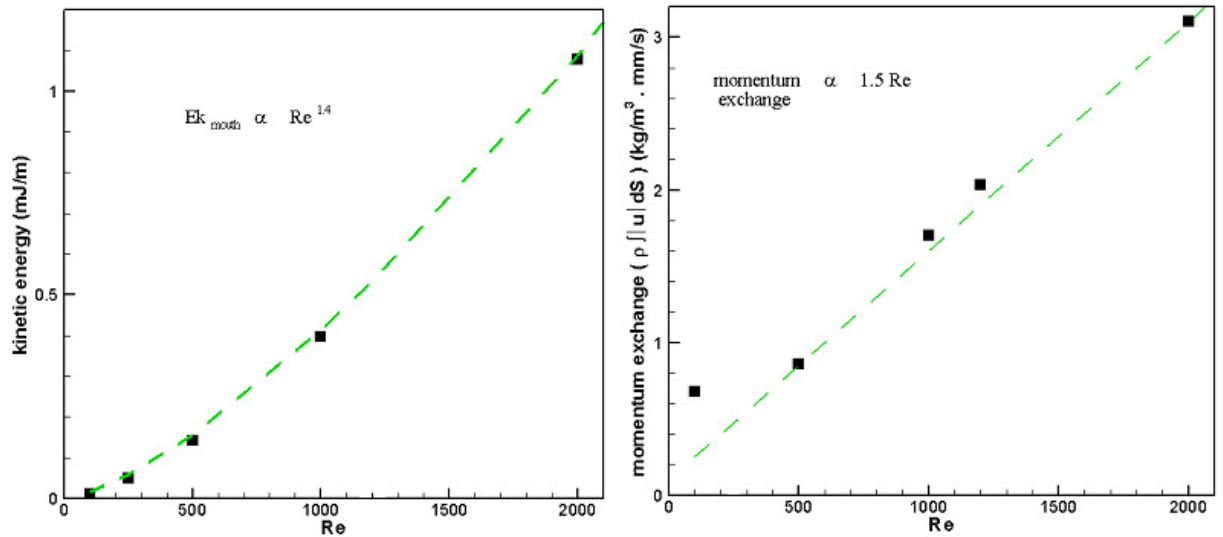
Figure 3.12. Fittings made to the kinetic energy and momentum exchange at the cavity mouth.

The total kinetic energy along the cavity mouth is shown in figure 3.13. This quantity is dominated by the streamwise velocity component, which is one order of magnitude greater than the wall normal velocity, with the spanwise component negligible. This is a measure of the entrainment of the channel kinetic energy into the vicinity of the cavity mouth. Here there is a non-linear relationship as Re is increased as it can be appreciated that on doubling Re the kinetic energy content of this plane is more than doubled. An exponent of 1.4 was found, see figure 3.12.
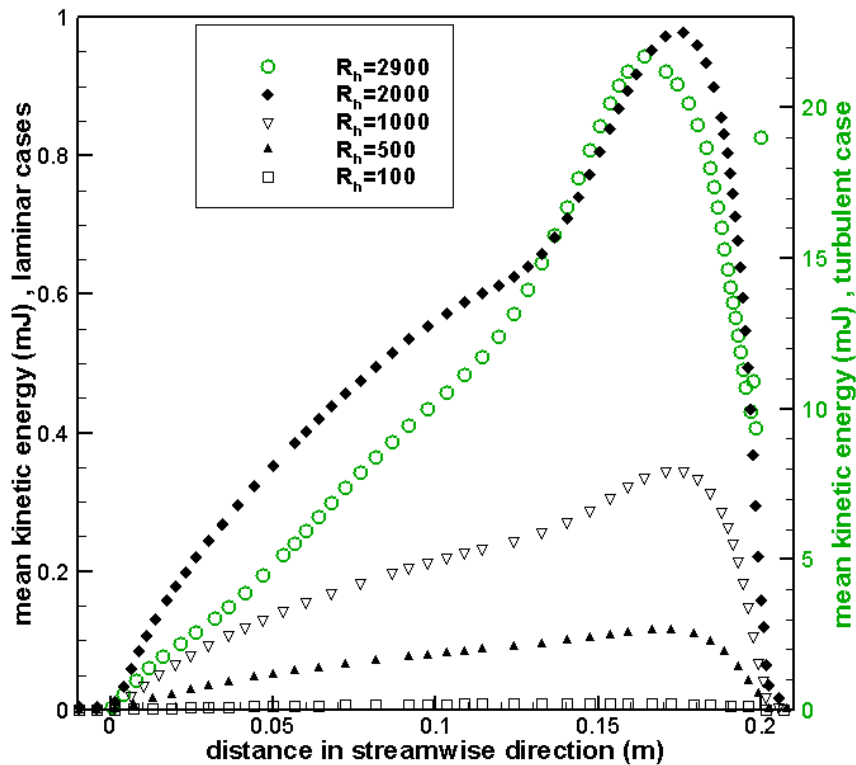
Figure 3.13. Dimensioned Ek kinetic energy across the mouth of the cavity.

34

3.1.7 Results: Flow Properties, Pressure/Streamlines, Turbulent

The computational domain for the turbulent case has the same dimensions as the laminar cases, with a greater resolution. The domain has 330x249x74 grid points and has been designed to match as closely as possible the indications for resolution requirements given by Mansour, Kim and Moin (1989). The maximum grid spacing in the x-direction, x^+=11.6 viscous units (based on the channel Re_{tau}=180) far from the cavity, reducing to x^+=1.44 at the cavity edges. In the wall normal direction the resolution is finer than one viscous unit in order to compensate for the increased drag caused by the cavity y^+=(0.83,4.12). In the spawise direction the grid spacing is uniform, z^+=7.85.

The resolution used here is generally better than that used by Mansour, Kim and Moin (1989), (x^+=17.7, y^+=4.4 (maximum at centre), z^+=5.9) except for the spacing in the spanwise direction. However, note that the previous case uses a Fourier/Chebychev method, thus the accuracy can be achieved with a lower resolution.

The initial velocity field for the channel is taken from a 2π fully developed turbulent channel simulation carried out using a pseudo-spectral method. Statistics for this field compare well with the database provided by Moser, Kim and Mansour (1999 & 1999 online). This 2π streamwise and spanwise periodic velocity field is repeated to fill the 4π channel-cavity domain, and the initial velocity in the cavity is set to zero. Due to periodicity and no-slip conditions at the wall, there are no discontinuities.

This 2π field is then used to generate a mass inflow at the inlet of the channel, and enters the domain at the bulk velocity of the turbulent field, see scheme in figure 3.14 of as discussed amoung several turbulent inlet conditions by Lund, Wu and Squires (1998). This method ensures a fully developed turbulent profile with excellent statistics, a comparison of data from the channel-cavity simulations with the database of Moser, Kim, Mansour (1999) is shown in figures 3.15-16, and temporal plots of kinetic energies for this case are shown in figure 3.16.
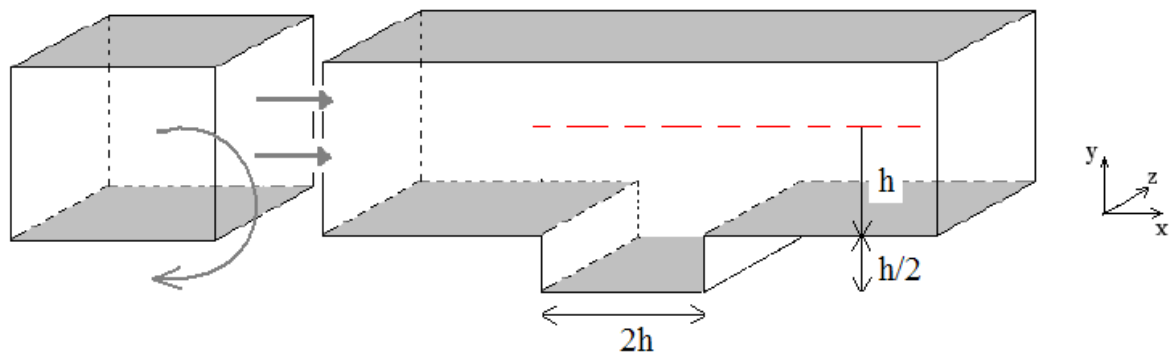
Figure 3.14. Scheme of the turbulent channel-cavity flow simulations with the auxiliary 2π input field.
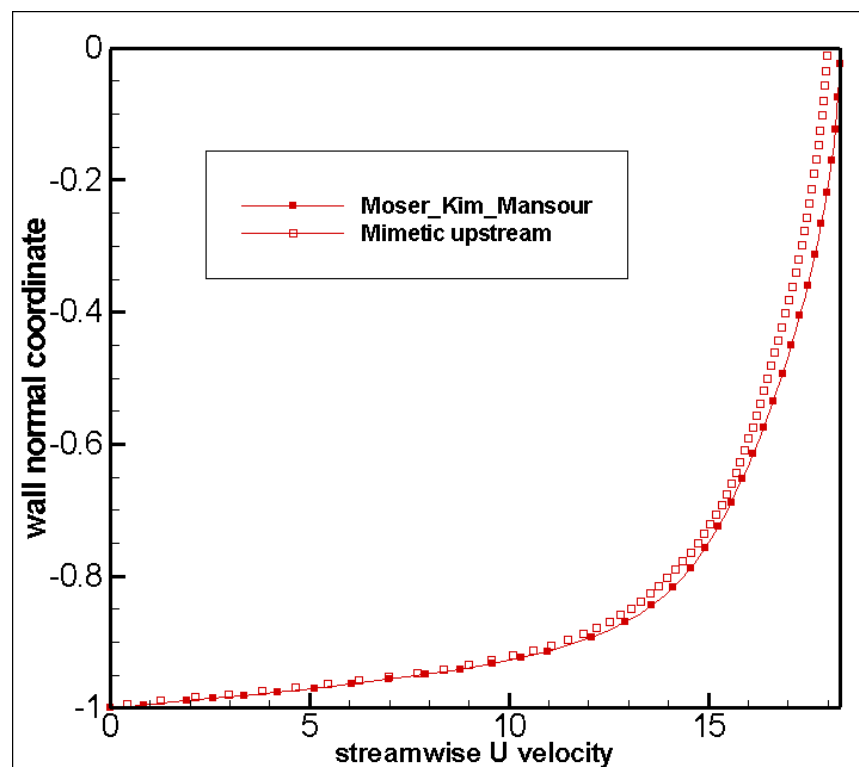

Figure 3.15. Comparison of the upstream U velocity profile for a section upstream of the cavity with the turbulent channel data of Moser Kim and Mansour (1999).
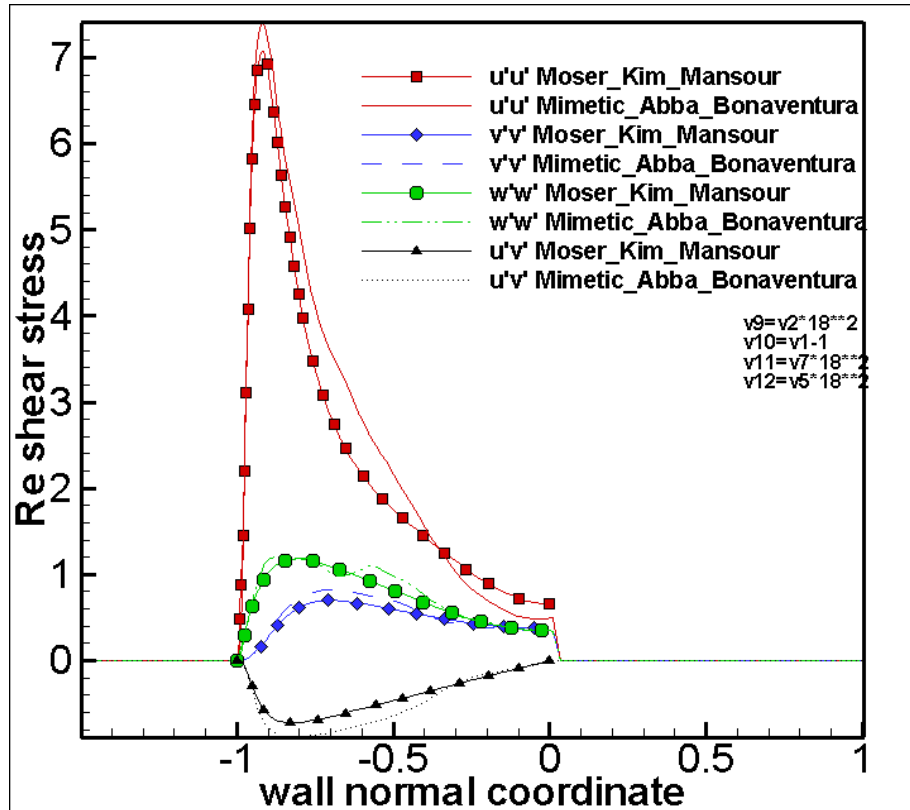
Figure 3.16. Comparison of Reynolds shear stress statistics for a section upstream of the cavity with the turbulent channel data of Moser Kim and Mansour (1999).

The statistics shown in figures 3.15-16 are generated from the turbulent channel in the upstream of the channel-cavity domain, after 60 time scales and averaged over 35 time scales. They are averaged in the spanwise direction, over approximately 4 streamwise length units, and over the channel centre. They appear to agree very well with the channel profiles of Moser, Kim and Mansour (1999), note however that the statistics provided by these authors are generated over a long time and over the whole length of a channel simulation. Here the domain includes a cavity, thus a small departure, indicating greater turbulence production is to be expected. In any case, these figures show that the upstream section of the channel has well developed turbulence with good statistics.

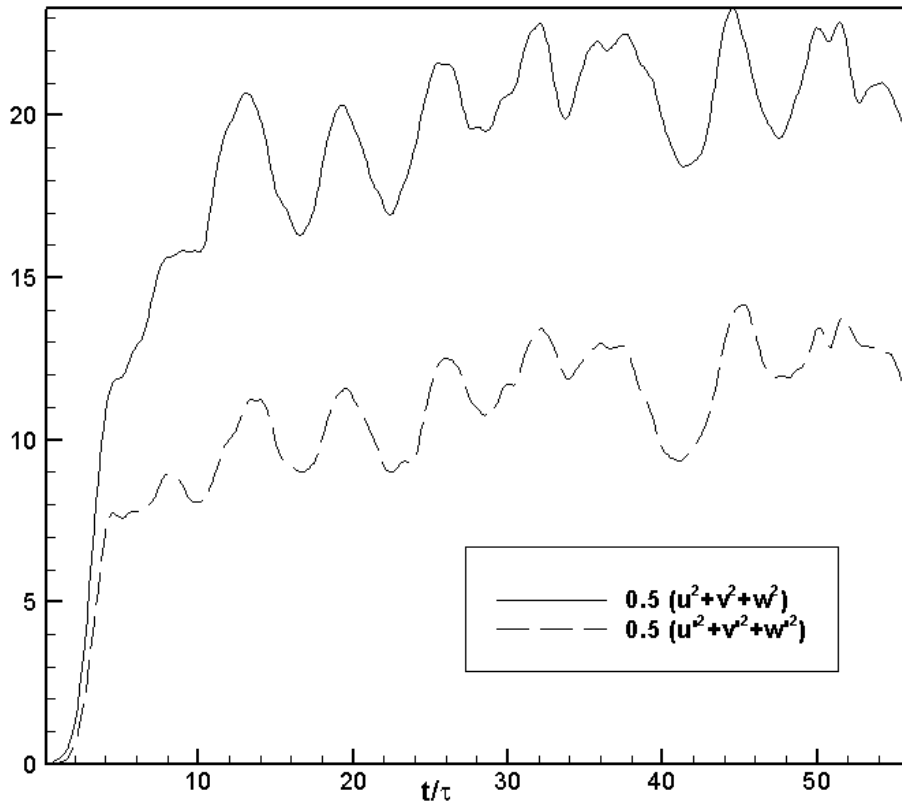$$\tau = \frac{h}{U_b} \quad (3.16)$$

Figure 3.17. Temporal plots of the total (u) and fluctuating (u') kinetic energies in the cavity volume.

In figure 3.8 the mean streamlines for this turbulent cavity flow can be seen. As was seen in the laminar cases a single primary eddy dominates the downstream half of the cavity, inducing a pressure low at its centre. In the upstream half of the cavity there is also the appearance of a further smaller secondary eddy, in agreement with the images from Grace, Dewar and Wroblewski (2004). It should be noted that this plot shows that the overall dynamics of the mean flow for both the laminar and turbulent cases are comparable.

The mean pressure along the mouth of the cavity is shown in figure 3,18. Close to the upstream edge there is a slight increase in the pressure, but the general trend over the cavity is a reduction, with a minimum in the region of the principal eddy in the downstream half of the cavity, before peaking at the downstream edge.
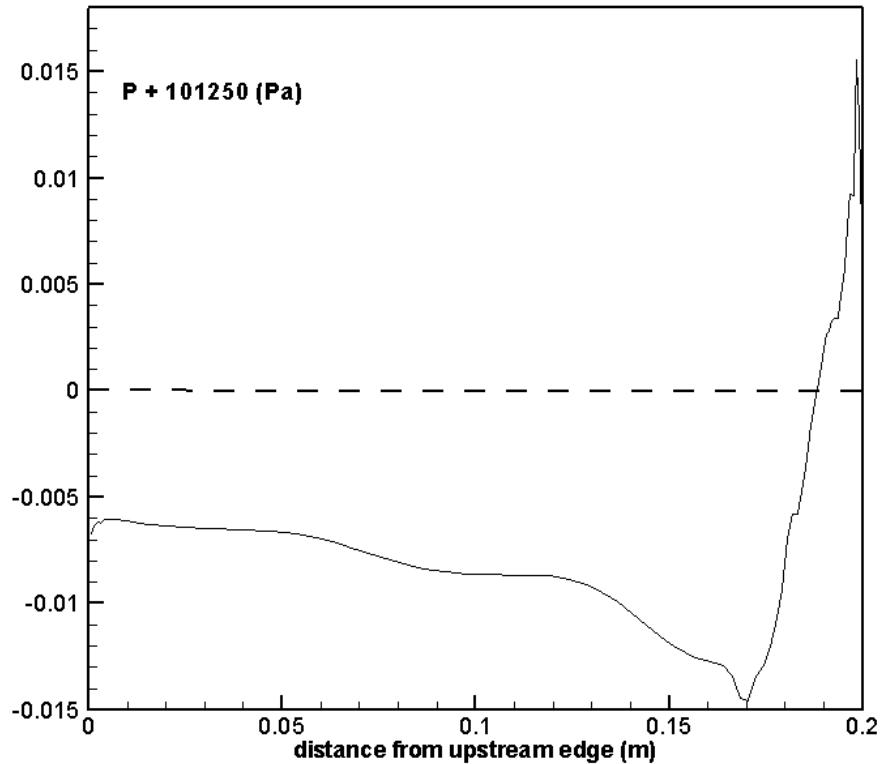
Figure 3.18. Mean pressure along the mouth of the turbulent cavity.

The mean velocity entering / exiting the cavity mouth is shown in figure 3.11. As in the laminar cases there is a relatively small momentum exchange in the upstream half of the cavity, with greater magnitude velocities confined to a smaller section close to the downstream edge. The velocities in the vicinity of the principal eddy in this case are much greater than those in the laminar counterpart, however here the exit velocity very close to the downstream edge is much greater than the velocity over the eddy.

In figure 3.13 the profile of mean kinetic energy over the mouth is plotted. It can be noted here that the kinetic energy increase, as one moves in the downstream direction, is smoother than in the laminar cases.
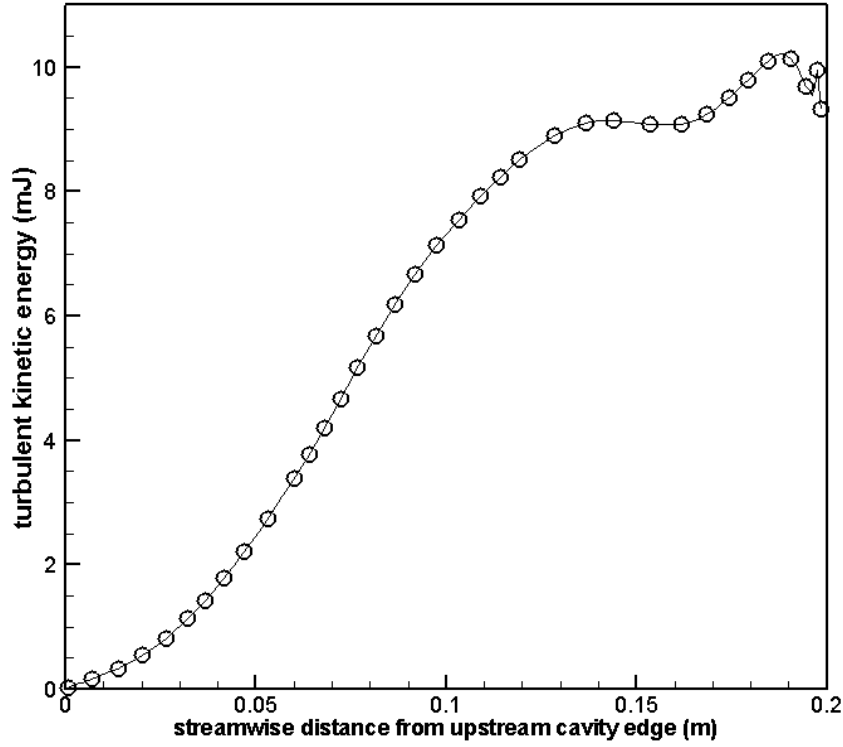
39

Figure 3.19. Profile of turbulent kinetic energy along cavity mouth.

In figure 3.19, the turbulent kinetic energy across the cavity mouth is shown. As the shear layer develops the fluctuation energy has the same increasing trend as the mean laminar and turbulent kinetic energy, until it reaches a plateau close to the downstream edge. Here the fluctuating kinetic energy remains relatively constant, before peaking again closer to the downstream edge.

Velocity vectors and the velocity magnitude, $\vec{v} = \sqrt{\left(u^2 + v^2\right)}$, within the cavity are shown in figure 3.20. The unit vector length is consistent through the laminar cases, allowing the relative movement of fluid to be seen throughout the cavity. The introduction of higher velocity fluid to the cavity on increasing Re can be observed, and it is interesting to note the great difference in magnitudes when the flow becomes turbulent.

In order to be able to better define the Reynolds number seen by the flow in the cavity, the mean velocity in the cavity volume, $\vec{v} = \sqrt{\dfrac{\sum\limits_{i=1}^{N}\left(u_N^2 + v_N^2\right)}{N}}$, has also been computed. Now considering the mean dimension of the cavity: (length+depth)/2=2.5, the new cavity local Reynolds number, Re_{cavity}, can be defined. See table 3.3 when the new range of Reynolds numbers is presented, based on the mean values from this analysis.

40

Re	Bulk channel velocity (mm/s)	Re_{cavity}	Cavity velocity (mm/s)
100	15.3	16.0	0.962
250	38.2	32.5	1.956
1000	152.9	100.0	5.996
2000	305.8	169.0	10.120
2900	459.2	1176.0	70.560

Table 3.3.   The Reynolds numbers of the channel and cavity, Re and Re_{cavity} respectively, and the corresponding dimensioned velocity.

Also visible from the table is the jump in values of the new Re_{cavity} range. On moving from Re=2000 to Re=2900, ie. incrementing Re by one half, we see almost an order of magnitude increase in Re_{cavity}. In the range $169 < Re_{cavity} < 1176$ the flow moves from the laminar to the turbulent regime.
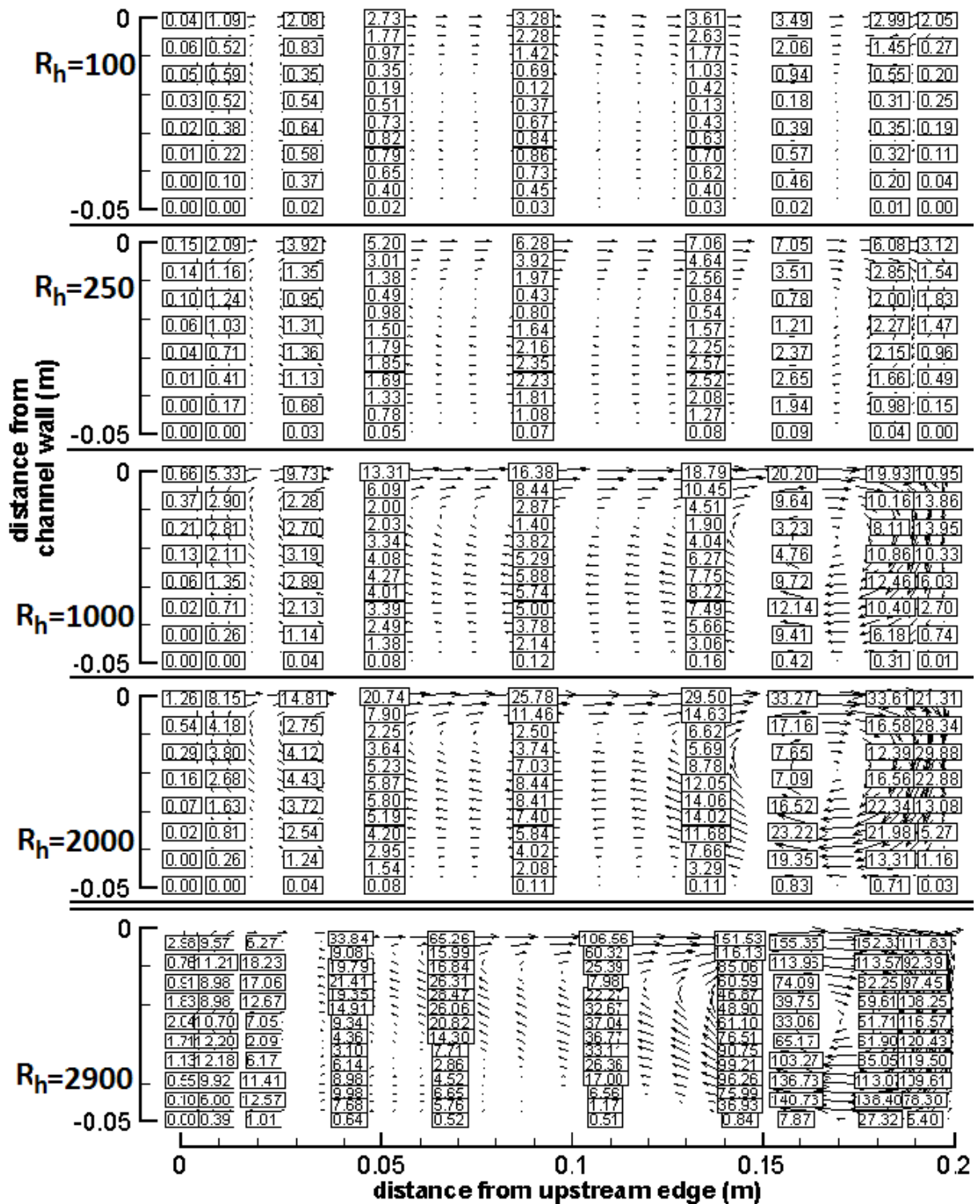
Figure 3.20. *Velocity vectors (u,v) and the value of* $\vec{v} = \sqrt{\left(u^2 + v^2\right)}$ *within the cavity. Vector lengths for the laminar cases, 100 < Re$_h$ <2000 are in proportion.*

42

Figure 3.23 shows two instantaneous images of the fluctuating u' component in two x-z planes within the domain. Figure a) is taken at y+20 from the top wall, the wall without the cavity. Here the high and low speed streaks, can be noted. Figure b) however is taken at y+20 from the wall including the cavity. Comparing these two figures one can immediately note the interference of the presence of the cavity upon these elongated streamwise structures. A greater difference between the high and low u' values can be noted and more confined pockets of perturbation as opposed to organized streaks can be seen downstream of the cavity.
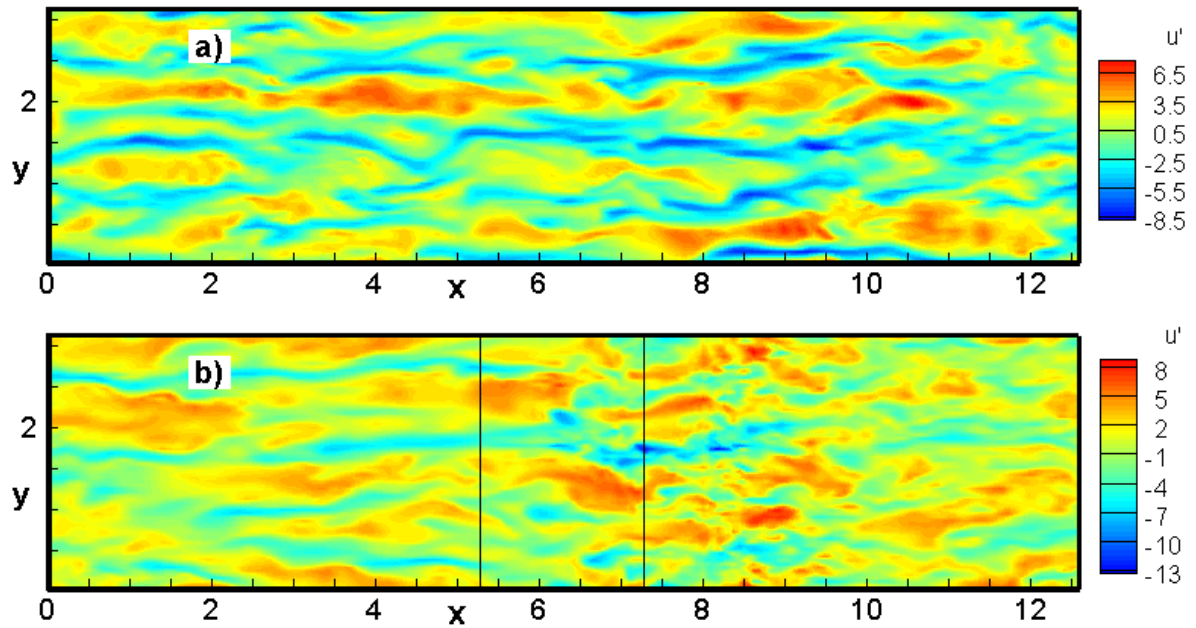

Figure 3.23. Contours of u'/u_tau at y+20 from the channel wall a) top of channel, b) bottom wall with cavity.

3.2.   Shearless Turbulent Mixing

In this chapter relevant concepts of homogeneous isotropic turbulence are first discussed before the presentation of the simplest turbulent mixing, namely a mixing of two homogeneous isotropic turbulence fields having only one inhomogeneous property between them. The transport properties of these fields are stated, before a study of the nature of the statistics of the turbulent transport in this mixing. The numerical methodology is briefly summarized and in the final chapter the energy balance and pressure-velocity correlation coefficient is derived.

3.2.1 Homogeneous Isotropic Turbulence, Important Considerations

A homogeneous and isotropic turbulence is the simplest type of turbulence. The assumption of non-directionality makes it a hypothetical flow, but its investigation allows us to understand the nature of fluid behaviour in all turbulent flows, and is particularly more apt in configurations which approach isotropy. Indeed due to its relative simplicity, it is the most investigated turbulence theoretically and experimentally, Hinze (1987).

The Velocity statistics of isotropic turbulence are Gaussian. In this configuration skewness (3.17), the third velocity moment, remains zero and the kurtosis (3.18), the fourth order moment, is 3 (flatness equal to zero). The only transport mechanism here is the turbulent and molecular diffusion, the Gaussian state indicating a lack of turbulent intermittence.

$$S = \frac{\overline{u_3^3}}{\left(\overline{u_3^3}\right)^{3/2}} \ (3.17) \qquad\qquad K = \frac{\overline{u_3^4}}{\left(\overline{u_3^2}\right)^2} \ (3.18)$$

3.2.2 The Mixing of Two Homogeneous Isotropic Turbulence Fields

The mixing of two homogeneous isotropic turbulence fields differing in only one property gives the simplest turbulent mixing configuration. This kind of mixing is characterized by the absence of a mean shear, thus there is no production of turbulent kinetic energy and no mean convective transport. It is therefore a decaying turbulence mixing in which all interaction is the result of the fluctuating pressure and velocity fields.

At high Reynolds numbers, for two mixing flows that are homogeneous and isotropic, each field can be defined by two parameters in Kologorov's theory, its kinetic energy and integral scale. In this investigation the two fields are identical apart from the kinetic energy content, thus setting up a ratio of energy across the mixing.

Figure 3.24 shows a scheme of this flow in which direction x is the homogeneous mixing direction.   Regions of high (E_1) and low (E_2) energy are separated by a mixing layer of thickness 2Δ.
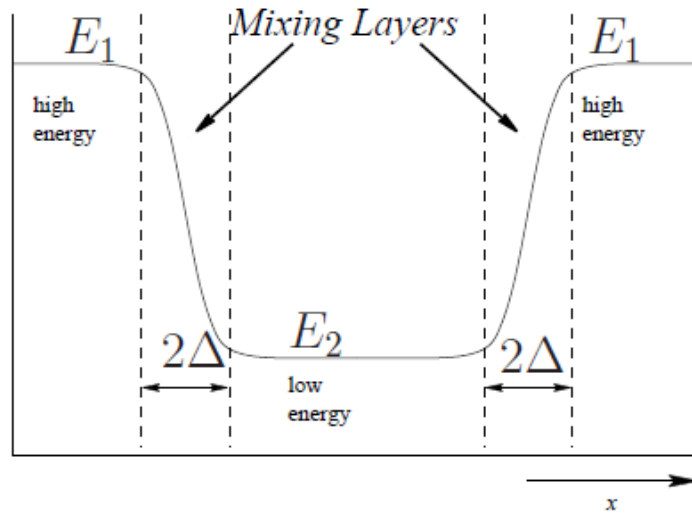
Figure 3.24. Scheme of the HIT mixing, E1 high energy and E2 low energy regions, separated by 2 mixing layers in the periodic domain.

It can be shown that the lengthscale of a turbulence field can be independent of its kinetic energy, thus it is possible to obtain, numerically, a dishomogeneity in the kinetic energy of two HIT fields while maintaining homogeneity in the lengthscale.

Normalising the integral scale by the kinetic energy (equation 3.19) makes it independent of the level of kinetic energy (see Batchelor, 1953, pg. 105). It is only dependent upon the energy distribution over the wavenumbers.

$$\ell = \frac{\int\limits_0^\infty u_i(x,t)u_i(x+r,t)dx}{u_i(x,t)u_i(x,t)} \quad (3.19)$$

Empirical investigations of this flow were first performed by Gilbert (1980) and Veeravalli & Warhaft (1989) (V&W) through the interaction of two passive grid generated turbulence

scales. These two wind tunnel investigations used perforated plates and bar grids, and had differing levels of success in attempting to induce a shear free mixing layer between two homogeneous and isotropic turbulence fields, due to the different experimental setups. They investigated both differing energy ratios and length scale ratios.

V&W found that the shearless mixing is non Gaussian, which was in contrast to the findings of Gilbert, who did not find such intermittency. V&W postulated that the likely cause of this difference in findings were the low ratios between the two interacting fields in Gilberts case, where the lengthscale and energy scale ratios were both less than 2.

In passive grid laboratory experiments the gradients of integral scale and kinetic energy are intrinsically linked. If the solidity of the mesh is changed, not only the lengthscale of the turbulence is altered, but also its energy scale. Numerical investigations have the advantage over the empirical investigators in that the turbulence properties can be individually controlled as discussed above. Such numerical investigations have been carried out by Briggs, Ferziger, Koseff and Monismith (1996), Knaepen, Debliquy and Carati (2004), Tordella and Iovieno (2006, 2007), Iovieno, Bailey and Tordella (2006), Bailey (2006), and by Tordella, Iovieno and Bailey (2007, 2008).

In these investigations, and in those of V&W, the mixing layer was seen to be intermittent and the velocity statistics non-Gaussian. It had been considered that as the lengthscale ratio approaches unity, thus for a single scale mixing, that the flow remains Gaussian. Briggs showed that this is not the case, albeit with a mild lengthscale ratio (0.93). Tordella (2007) went on to characterise the effect of the concordance or opposite of the lengthscale/energy scale ratios, finding that mixing penetration was enhanced when the ratios were concordant and lower where they are opposite.

The work of V&W was fully reproduced numerically by Knaepen, but working at higher Reynolds number. This work showed that the flow Reynolds number has little if any effect on the results.

The state of the art has now moved on to active-grid control techniques, in which the energy and length scales in the turbulence fields can now be better controlled through actuators placed on the bar grid. An example of the initial studies of the decay of isotropic turbulence using such grid agitation is that of Ling and Wang, (1972), with more modern works using these techniques from Kang, Chester and Meneveau (2003), Kang and Meneveau (2008).

3.2.3 Methodology

The computational frame is a parallelepiped domain with periodic boundary conditions in all directions. In this infinite domain the Navier-Stokes equations (equation 2.1) are solved with a with a fully dealiased (3/2 rule) Fourier-Galerkin pseudospectral method. Time integration is performed using a fourth order explicit Runge Kutta scheme. A parallelised version of the code is presented in Iovieno, Cavazzoni and Tordella (2001).

The initial conditions are generated from a $(2\pi)^3$ homogeneous isotropic velocity field taken from Wray (1998). To create the initial condition, the velocity field is repeated creating a 4π $(2\pi)^2$ domain. In one side of the domain, each velocity component is multiplied by a constant, creating a ratio of energy between the fields, but keeping similar spectra thus introducing no ratio of scales. A hyperbolic tangent function is then used to smooth the interface and to define the initial mixing layer.

Tests were performed for domains of dimension 4π x $(2\pi)^2$ with 256x128^2 grid points and with an initial mixing layer representing 1/40 of the inhomogeneous dimension (largest grid dimensions in the mixing inhomogeneous direction). Further tests with dimensions 8π x $(2\pi)^2$ and 512x128^2 points and initial mixing layer 1/80 of the inhomogeneous dimension were performed to verify the numerical accuracy. Due to periodicity, two mixing layers are actually simulated, all subsequent results are averaged over these two layers.

For high Reynolds numbers the two turbulence fields decay algebraically with the same decay exponents, thus the initial ratio of energy remains constant throughout the whole mixing process, see figure 3.25, where the temporal decay is shown for energy ratios 6.7 and 12.1, with their initial spectra in the inset.
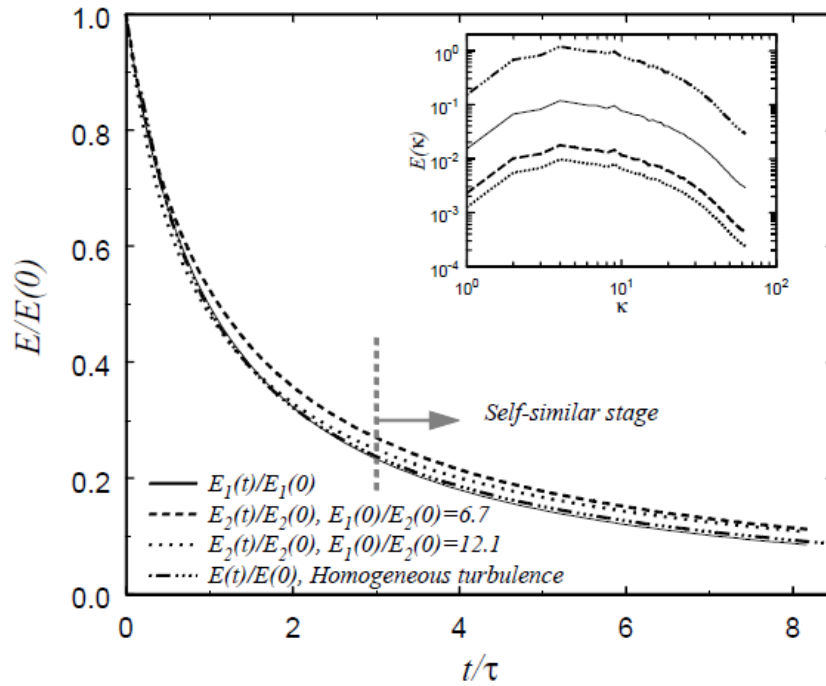
Figure 3.25. Turbulent kinetic energy decay of the interacting fields, and inset, initial energy spectra.

3.2.4 Results: Intermittency, Asymptotics and Gaussian State

It was previously thought, and with well founded reasoning, that a HIT mixing devoid of a lengthscale ratio would behave as a single HIT field in that it would not mix and would not show intermittence. Results from these numerical simulations show that on the contrary, in these conditions, the mixing can be highly intermittent and that this intermittence is dependent on the energy ratio ε.

The fluctuating velocity component u is responsible for the transport across the mixing. The moments of this component are analysed in order to determine the level of intermittency. Figure 3.26 shows the skewness in the inhomogeneous x direction for the mixing with energy ratio of $\varepsilon = 100$. External to the mixing layer, in the isotropic field (high energy on the left), it can be seen that skewness vanishes, remaining zero. Closer to the centre of the mixing there is a departure from zero skewness, peaking on one side of the mixing centre.

Also shown in figure 3.26 is the penetration, η. The penetration is the extent to which one turbulence field has encroached into the other, and signals the location of the largest intermittent bursts. Here the high energy side from the left side of the mixing center has penetrated into the low energy side of the mixing.
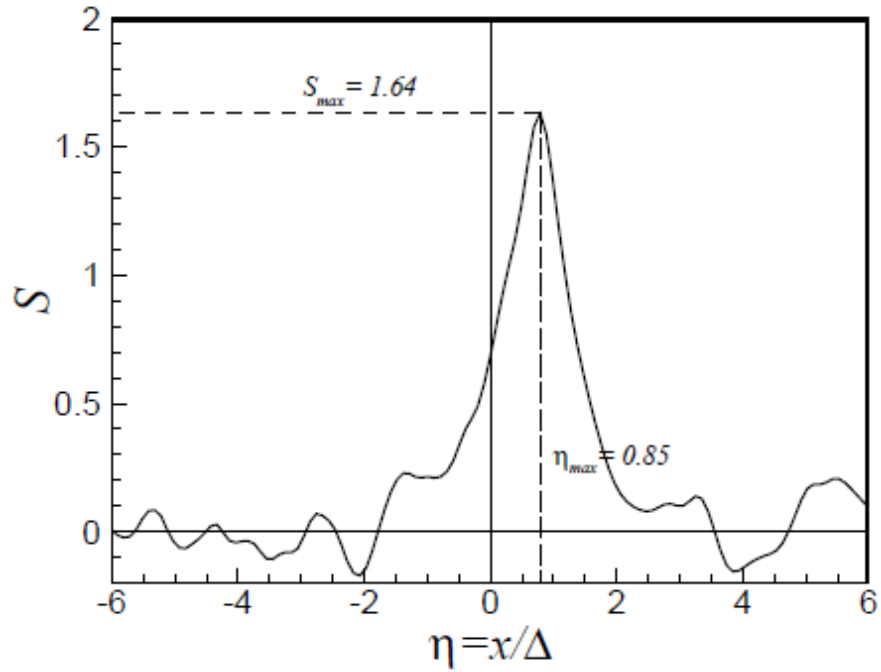
Figure 3.26. Typical profile of skewness across the mixing direction, x axis has been normalised by Δ, the conventional mixing layer thickness. The energy ratio here is 100, at t/t_tau=3.5.
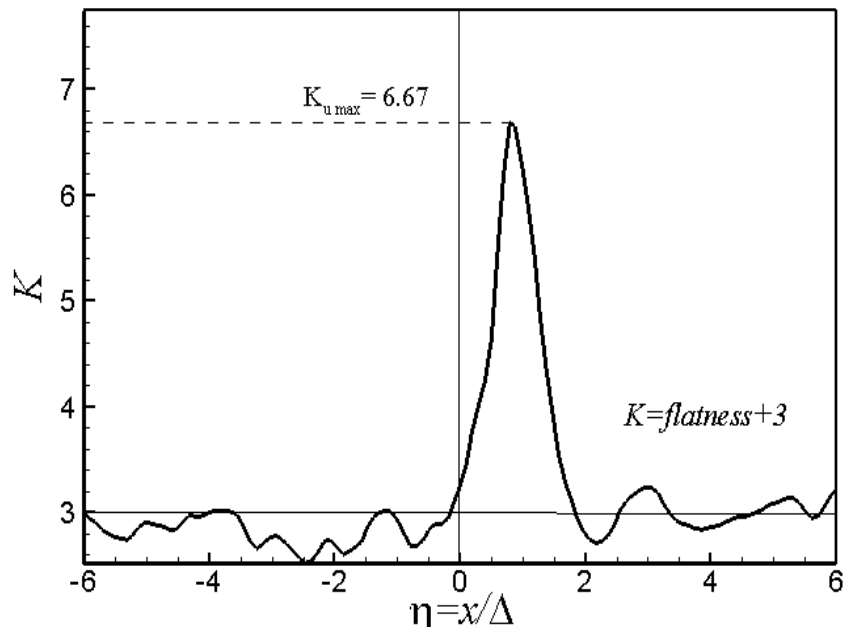

Figure 3.27. Typical profile of the kurtosis across the mixing direction, x axis has been normalised by Δ, the conventional mixing layer thickness.

The time dependent maximum of the skewness for four cases is presented in figure 3.28, and for kurtosis in figure 3.29. After approximately 3 eddy turnover times, less for the lower energy ratio cases, the maxima have ceased to rise. At this stage the turbulence has entered a

self-similar state of decay. Statistics are calculated from this self-similar stage, thus discarding the initial transient.

Also shown in figures 3.28-29 are the time evolution of the maxima of skewness and kurtosis from the V&W experiments. Here the spacial evolution in the laboratory has been converted to a temporal decay using Taylor's hypothesis, based on the wind tunnel mean flow velocity and distance from the grid. Note that the energy ratios of the empirical data are much lower than those of the numerical data owing to the physical limitations of the lab experiments. There is a good agreement in the initial development of the mixing, as well as the post transient behaviour.
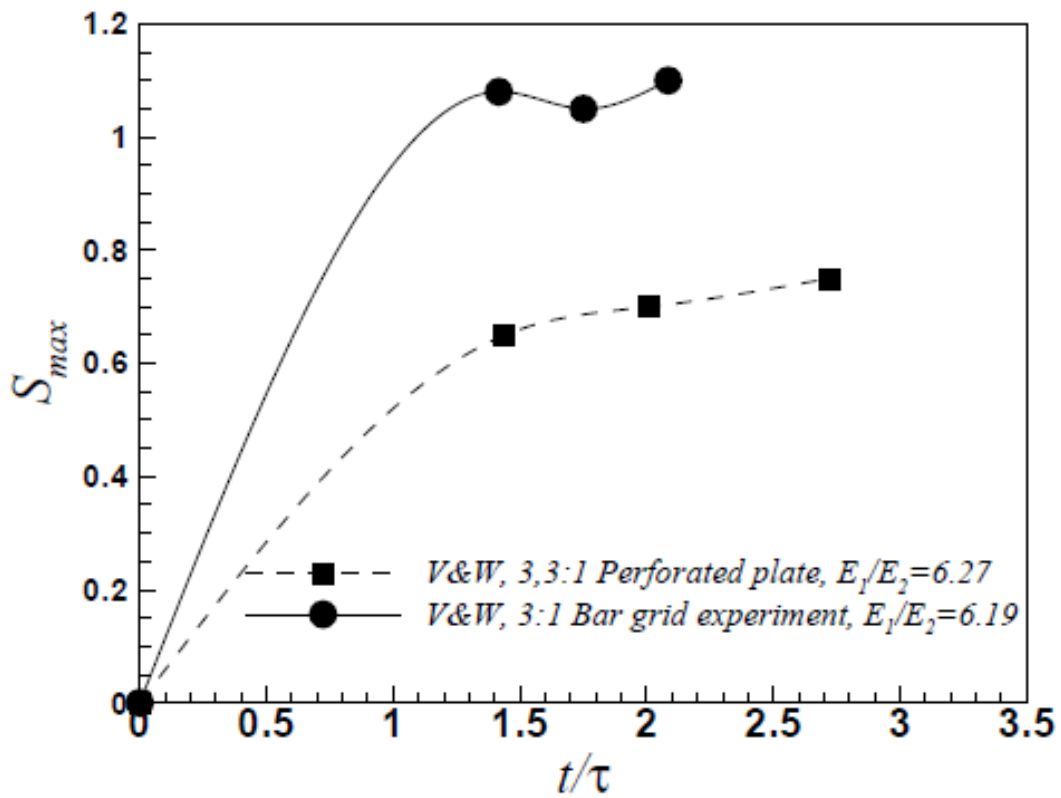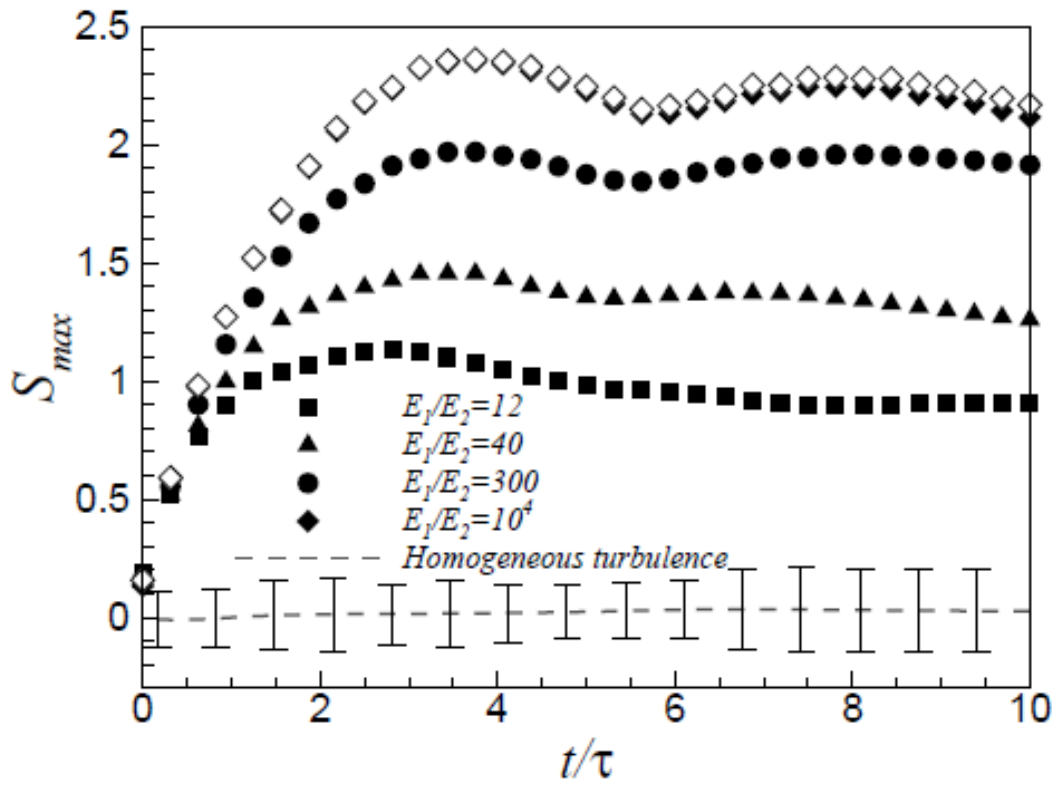
Figure 3.28. Temporal evolution of the maximum of the skewness. a) for four energy ratios in the numerical simulations. b) experimental data from the lab experiments of Veeravalli and Warhaft (1989).
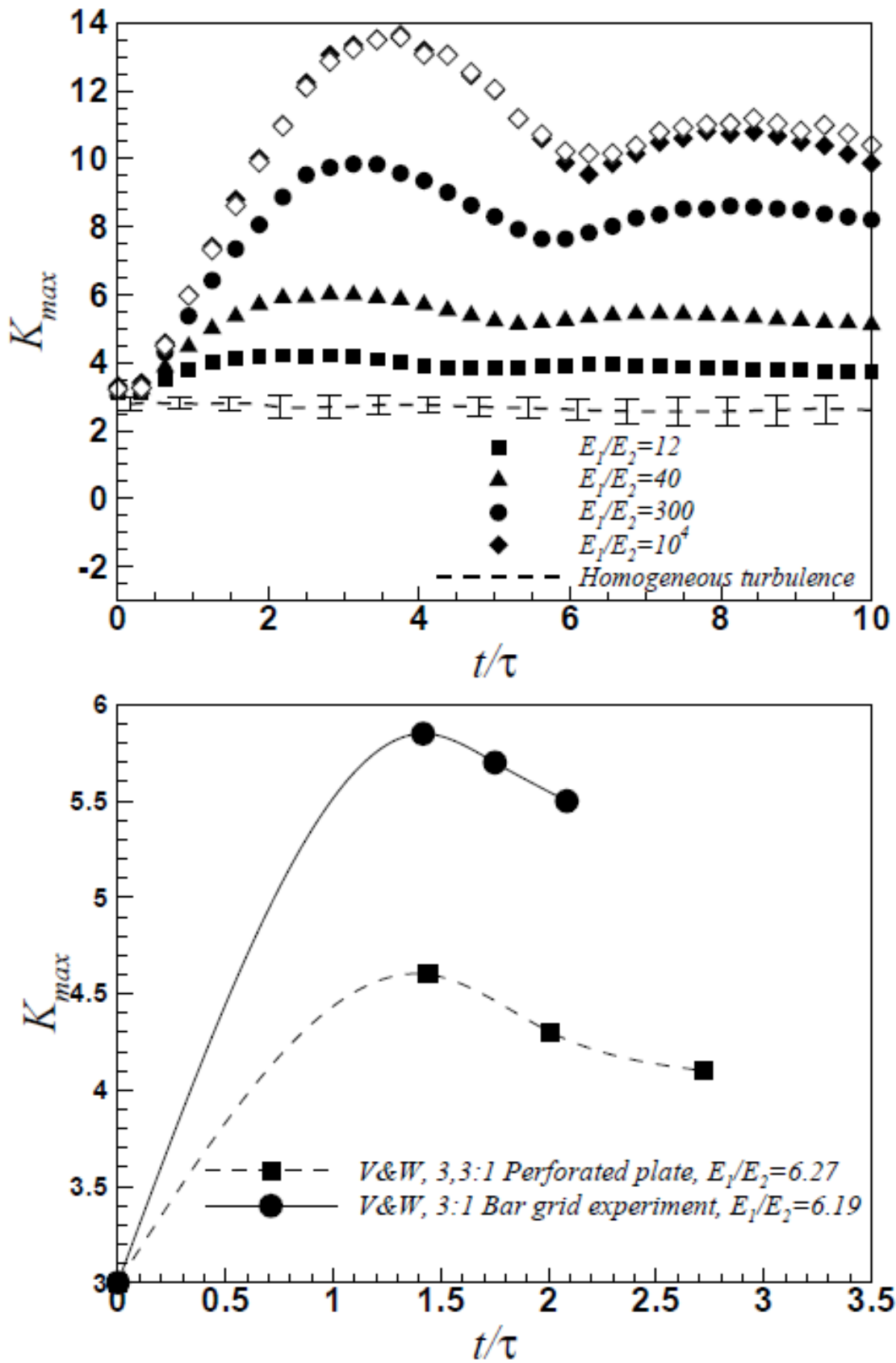
Figure 3.29. Temporal evolution of the maximum of the kurtosis. a. for 4 energy ratios in the numerical simulations. b. experimental data from the lab experiments of Veeravalli and Warhaft (1989).
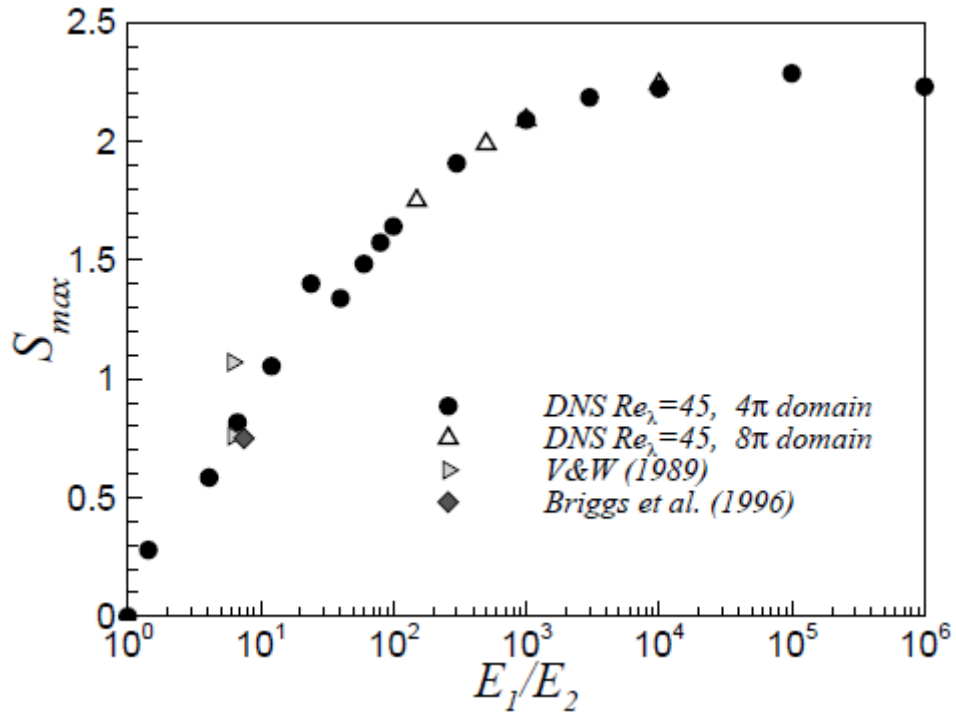
Figure 3.30. Maximum of the skewness as a function of the initial energy ratio, data from 4π and 8π simulations, lab experiments of Veeravalli and Warhaft, and numerical simulations of Briggs.
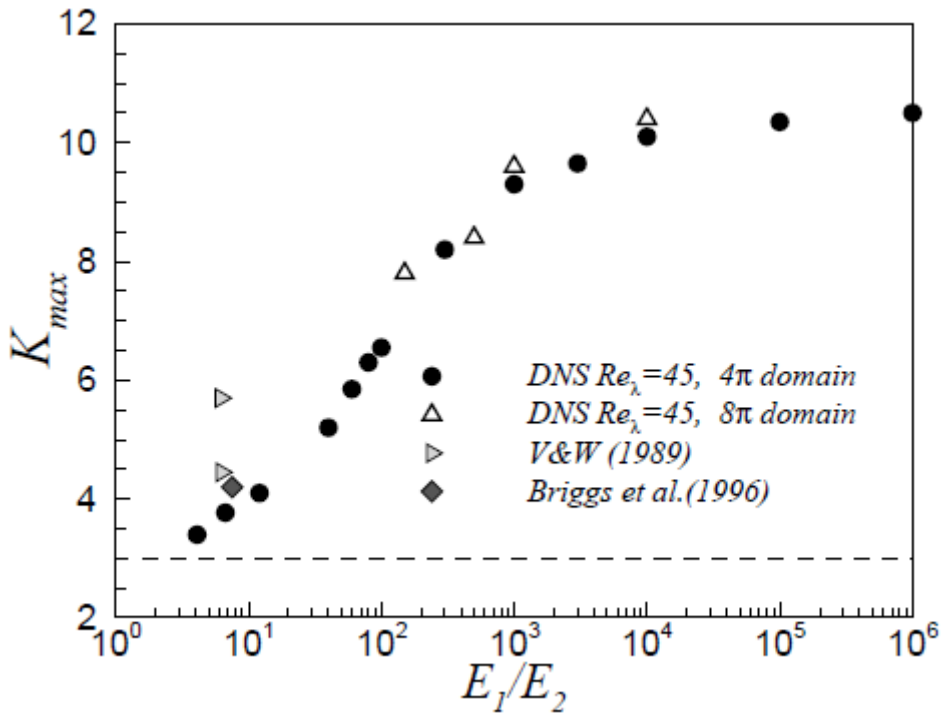

Figure 3.31. Maximum of the kurtosis as a function of the initial energy ratio, data from 4π and 8π simulations, lab experiments of Veeravalli and Warhaft, and numerical simulations of Briggs.
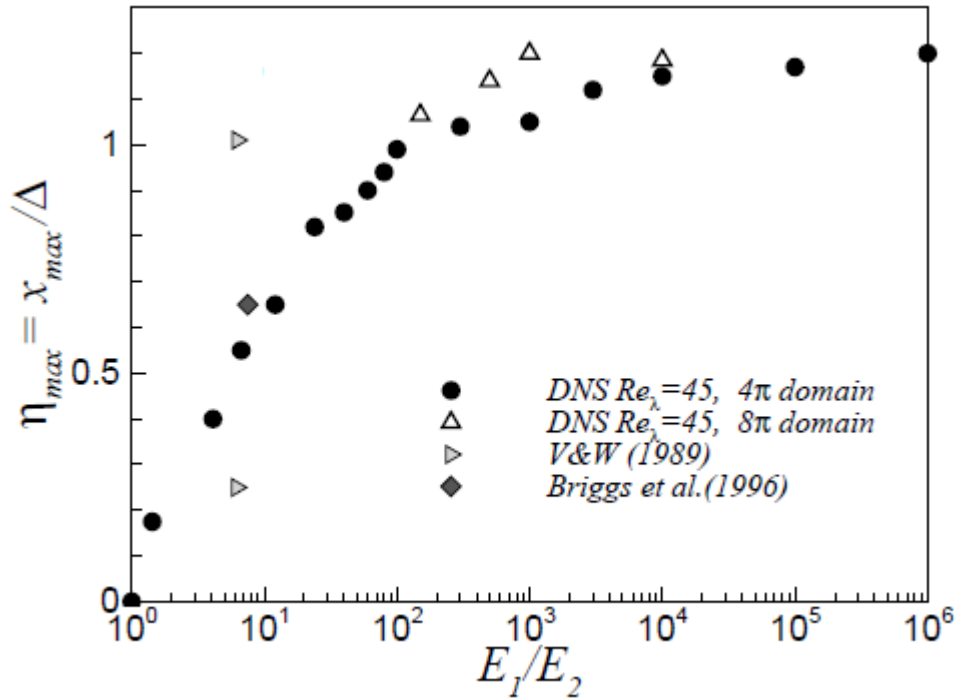
53

Figure 3.32. Normalised position of the maximum of the skewness in the mixing layer as a function of the initial energy ratio, data from 4π and 8π simulations, lab experiments of Veeravalli and Warhaft, and numerical simulations of Briggs.

The maximum of skewness as a function of energy ratio is plotted in figure 3.30, for energy ratios in the range $E_1/E_2 \in (1, 10^6)$. This plot consists of data from the regular 4π x $(2\pi)^2$ as well as the more highly resolved domain 8π x $(2\pi)^2$, a collapse of the data onto a single curve is evident, thus confirming the sufficient grid resolution. Below 10^2 the maximum scales almost linearly with the logarithm of the energy ratio, and for higher ratios it can be seen that an asymptotic limit has been shown. Also plotted here are empirical data of Briggs and V&W which are in good agreement with the low energy ratio results. Note that a small difference is likely to occur since in the V&W experiment the scale ratio was not 1.

The maximum in kurtosis, plotted as a function of the energy ratio, figure 3.31, reaches very high values with respect to the Gaussian value of 3, indicated by the dashed line. This signifies the presence of extremely intense intermittent events. The location of these events, indicated by the normalised penetration, figure 3.32, is in the low energy side of the mixing. Indeed from this figure a maximum of 1.2 is obtained for energy ratios from 10^2 to ∞. The penetration is the instantaneous distance from the initial mixing centre, normalised by half the instantaneous mixing layer thickness. A value of 1.2 is therefore a considerable penetration of the high energy field into the low energy.
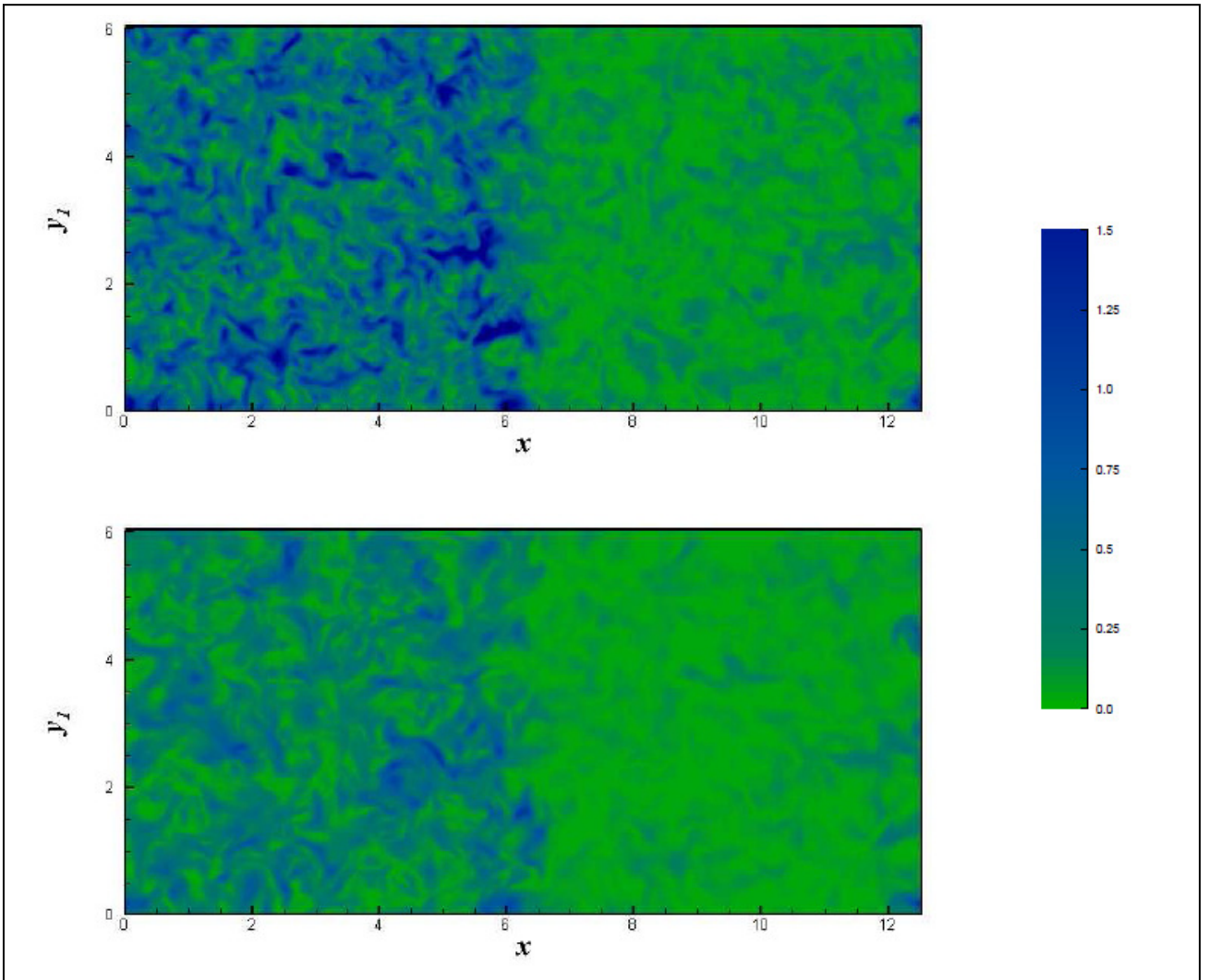
Figure 3.33. Contours of kinetic energy at two time instants for E1/E2=6.7, top. t/τ=0.8, bottom t/τ=2.5.

4. Energy Balance in Sheared and Shearless Flows

Chapter 4 looks in depth at the energy balance for the two flow configurations considered. Continuing the analysis of the cavity profiles, the products of the pressure and velocity are now considered together at the cavity mouth. In section 4.1 the mean energy balance in sheared laminar and turbulent cavity flows can be found, and in section 4.2 the fluctuating energy balance is presented. In the final section 4.3 the energy balance in the shearless turbulent mixing is considered. The integral of the pressure and kinetic energy transports across the respective interaction surfaces are determined before developing the energy balance in each section.

4.1. Mean Pressure/Kinetic Energy Transport for Cavity Flows

Continuing the analysis of the flow properties at the mouth of the cavity, we now turn our attention to forming the products which make up the transport terms, their integral and the relation between the pressure and kinetic energy transports. The product of the pressure and wall normal v velocity at the cavity mouth is depicted in figure 4.1 for the laminar cases Re=100, 500, 1000 & 2000, and the turbulent case Re=2900. For all cases it can be seen that the greatest proportion of pressure transport is in the region of the downstream forward facing step of the cavity, with a comparatively small magnitude pressure transport along the rest of the cavity. The profile very much takes its form from the velocity profile found in figure (3.12).
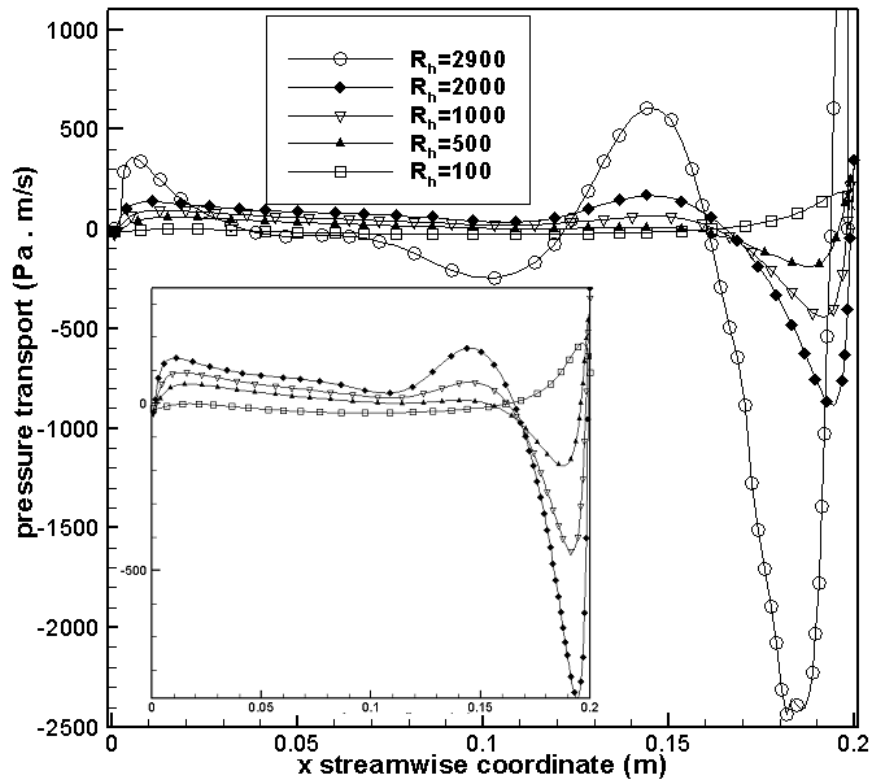
***Figure 4.1. Dimensioned pressure transport across the cavity mouth for a range of Re,
insert omitting the turbulent case.***

It is interesting to note that the most significant acoustic emissions from cavities are associated with interactions at the downstream edge, Howe (2004). Figure 4.1, even though some of the flows depicted are laminar steady, which are intrinsically silent, Colonius (2004), shows immediately where the greatest interaction between the velocity and pressure fields is located.
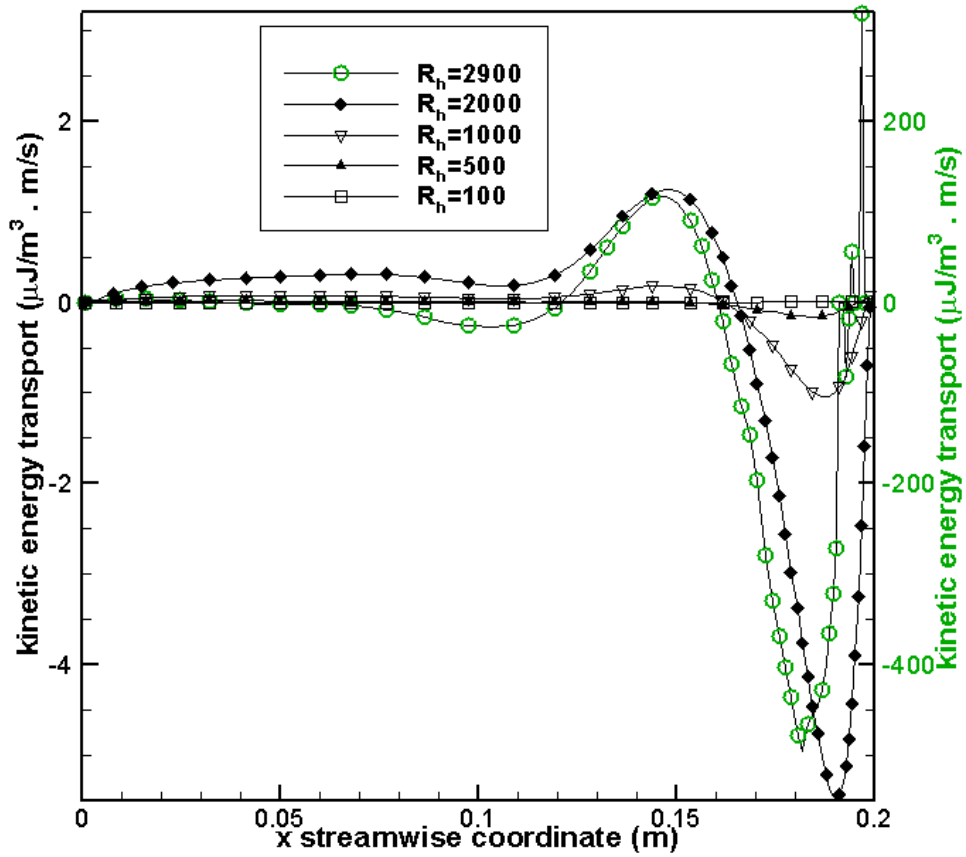
Figure 4.2. Dimensioned kinetic energy transport across the cavity mouth, left ordinate for the laminar cases, right ordinate turbulent case.

In figure 4.2 the kinetic energy transport along the mouth of the cavity is depicted. The shape of the graph resembles that of the wall normal v velocity graph. Most of the energy transfer takes place in the downstream half of the cavity. In all cases the kinetic energy transport increases moving downstream owing to the greater streamwise velocity in this plane, and for Re 500 and greater it can be seen that the greatest magnitude transport occurs close to the downstream edge for the laminar cases. The negative peak in kinetic energy transport in the turbulent case can also be found in the same region, however the maximum transport in the turbulent case is a relatively very high magnitude outflow very close to the downstream edge.
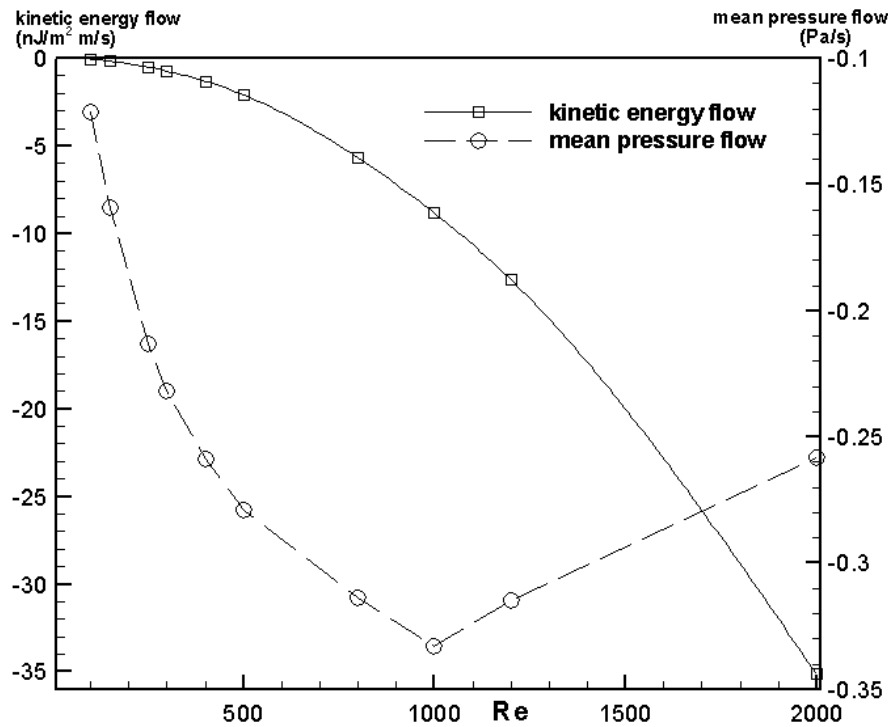
Figure 4.3. Dimensioned integral of the kinetic energy and pressure transports over the range of Re 50 to 2000.

In figures 4.3 the total dimensioned pressure and kinetic energy transports are plotted as functions of Re. In both cases the graphs are always negative, indicating that there is a flow of mean energy and pressure into the cavity.

The kinetic energy transport can be seen to continually increase in magnitude with Re, indeed as Re is doubled the transport is more than doubled, this is as a direct consequence of the increased kinetic energy entrained into the cavity mouth area as seen in the previous plots, figure 3.13.

The pressure transport however reaches a maximum around Re=1000 and is then seen to reduce if Re is increased further. Figure 4.1 showed that the strength of the pressure transport increases with Re, despite this it can be seen in figure 4.3 that the net transport of pressure remains relatively constant. Increasing from Re=1000 the increase in pressure outflow from the cavity is evidently greater than the increase in the inflow.

Considering now the ratio between these two transports for the laminar and turbulent mean flow, alpha, equation 2.9, is shown as a function of Re in figure 4.4. It can be seen that for increasing Re, whether laminar or turbulent, this coefficient tends to an asymptotic limit, signifying that for high Re there is a common ratio between the mean pressure and kinetic energy transports.

59

The asymptote is reached where Re exceeds 2000. It is around this Re that the first instances of unsteadiness can be expected in this flow. On incrementing Re further the flow will become transitional, where pockets of agitated flow, or turbulent structures will begin to appear. It is at this stage that the cavity flow starts to emit noise since, as discussed by Howe (2004), these structures impinge of the downstream edge, causing a time disturbance to the pressure field. When the flow transitions to turbulent the generation of the structures is more frequent and they usually have more energy, and thus the pressure disturbance greater. This set of phenomena, unsteadiness, transition and turbulence appear when the asymptote is reached.
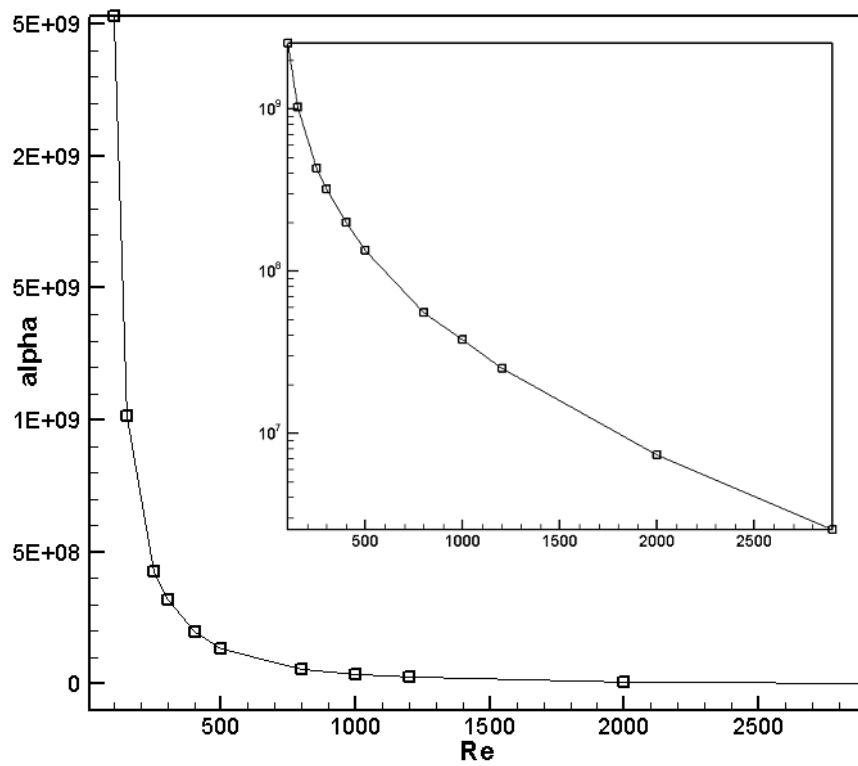

Figure 4.4. Ratio between pressure and kinetic energy transports.

4.2. Fluctuating Pressure/Kinetic Energy Transport in the Channel Cavity Flows

In this section we will first consider the fluctuating transports in the whole flow domain, before then concentrating on the balance close at the cavity mouth. Figure 4.5 shows the

60

profile of the modulus of the fluctuating pressure and kinetic energy transports in a section of the channel flow upstream of the cavity, equations 4.1-2.

$$\sqrt{\overline{(p'v')^2}} \quad (4.1) \qquad\qquad \sqrt{\overline{\left(v'\frac{u_i'u_i'}{2}\right)^2}} \quad (4.2)$$

The total transports are zero at the wall and close to zero in the centerline region, close to the wall they reach a peak however. The cavity is located on the bottom wall at y=-1. It can be seen that the turbulent transports are almost 50% greater on the lower side of the channel centerline. This shows that the cavity has some upstream influence on the fluctuating components on the lower side of the channel.
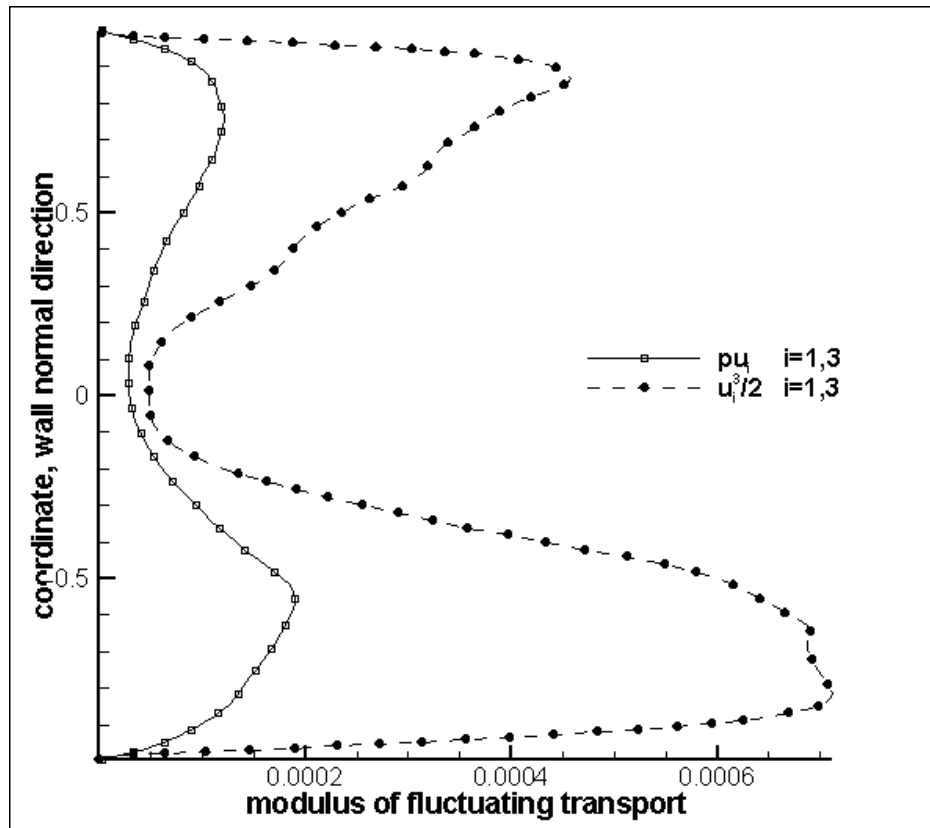

Figure 4.5. Magnitude of the total pressure and kinetic energy
transports in the channel upstream of the cavity.

Figure 4.5 shows that in the channel the pressure transport is always less than kinetic energy transport, and that in the centerline region it represents its greatest proportion, however in this location both transports are relatively low. At the channel centre, the convective transport is the greatest transport, thus the combined sum of the pressure and kinetic energy

transports is globally less significant. In general the pressure transport is 20% ± 10% of the kinetic energy transport in the rest of the profile, ie. it is secondary to the kinetic energy transport and is in agreement with the discussion of Yoshizawa (2002).

The turbulent kinetic energy transport along the cavity mouth is shown in figure 4.6. The overall trend is for a flow of fluctuation energy into the cavity, reaching a peak upstream of the location of the principal eddy. There is then a confined outflow close to the downstream edge.
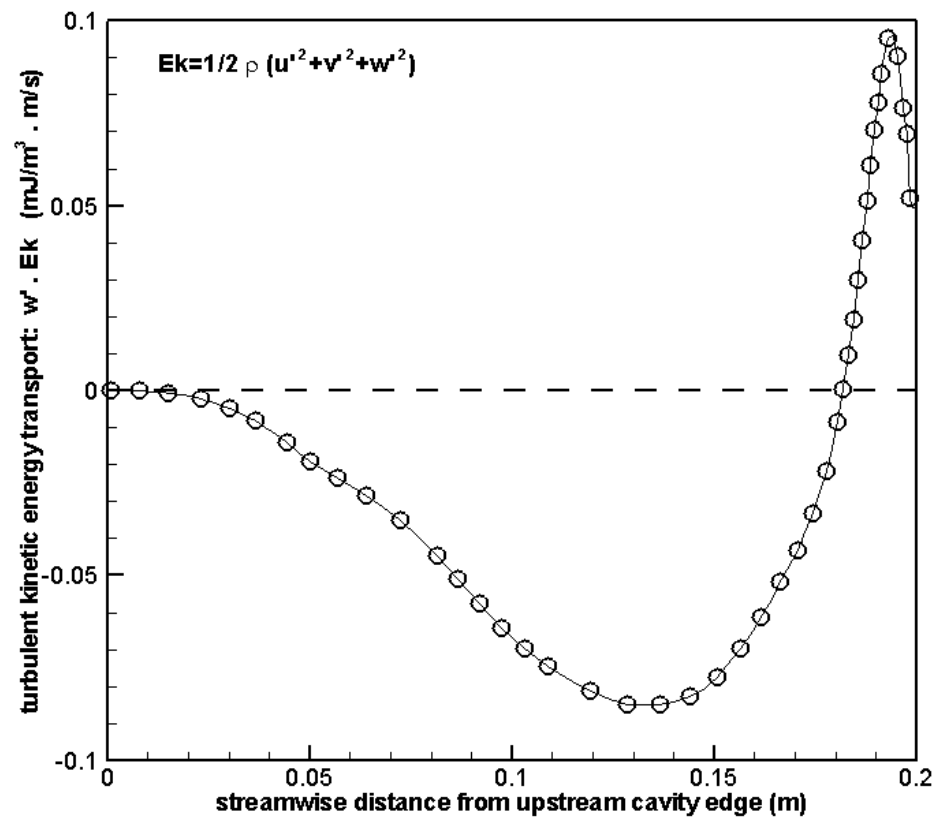

Figure 4.6. Profile of turbulent kinetic energy transport along cavity mouth.

On the other hand the fluctuating pressure transport, shown in figure 4.7, oscillates between positive and negative values moving downstream, with increased intensity close to the downstream edge. **Alpha for the fluctuating transport at the cavity mouth was calculated to be 0.58.**
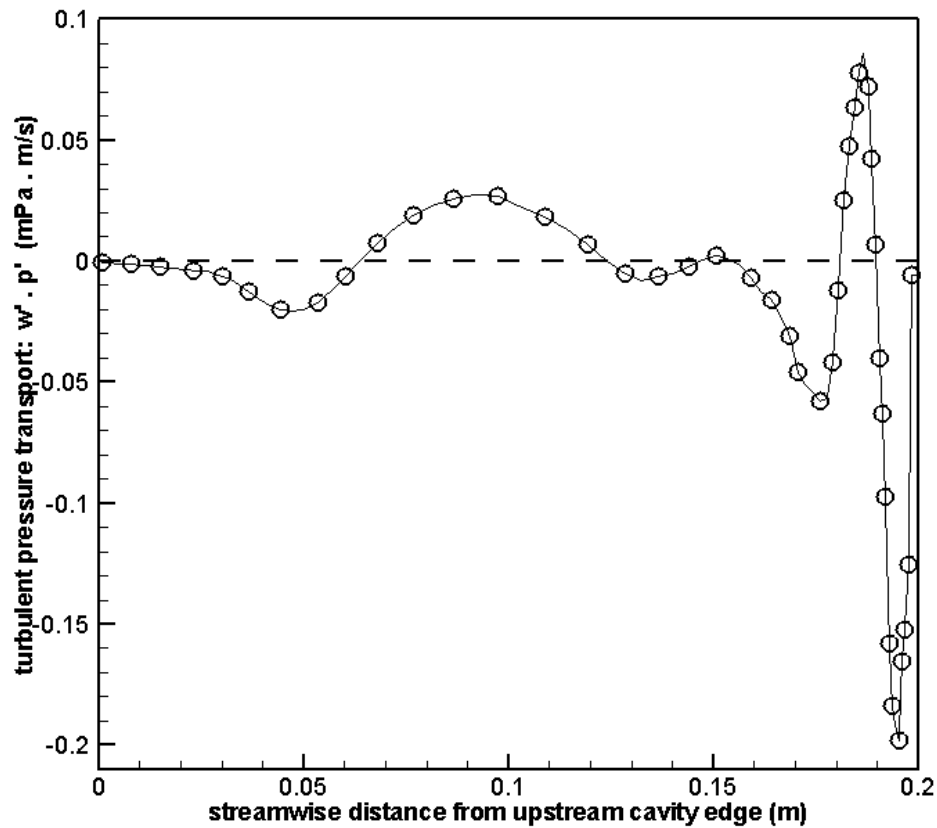
Figure 4.7. Profile of turbulent pressure transport along cavity mouth.

4.3. Pressure/Kinetic Energy Transport in Shearless Turbulence Mixings

In the initial condition we have a homogeneous isotropic turbulent mixing with one inhomogeneous property and no mean transport between the two turbulence fields exists. On analysing the 2nd and 3rd order moments it can be seen that a transport develops, leading to an anisotropic velocity field, see figure 4.8..

This configuration represents a flow from which we can make fundamental conclusions about the development and interaction of turbulent transports. The flow is free of mean shear and scale ratio, thus no production of turbulent kinetic energy. The only interactions are those between the fluctuating pressure and velocity fields. Under these conditions a universal relation between the pressure transport and the kinetic energy transport for varying energy ratios across the mixing has been found. For this HIT mixing at Re_λ =45, **alpha has been determined to be 0.37**, and thus the pressure transport is not dominated by the kinetic energy

transport. In addition, it has been seen that the pressure transport is in the opposite direction to the kinetic energy transport.

Now comparing the current result and that of the previous section, where alpha was determined to have a value of 0.58, we are able to attribute some of the differences. We can also consider the turbulent cavity flow as the mixing of two regions differing in energy content. The energy ratio between the cavity and a volume of equal size in the channel was determined to be $E_1/E_2 = 15.39$, which lies within the range of energy ratios considered for the shearless mixing, $E_1/E_2 \in (1, 10^6)$. When moving from the shearless HIT mixing to that of the turbulent cavity flow, the increased molecular level transport resulting from the introduction of shear is seen to augment the relative importance of the pressure transport. Indeed shear introduces greater recirculation into the cavity mouth region.
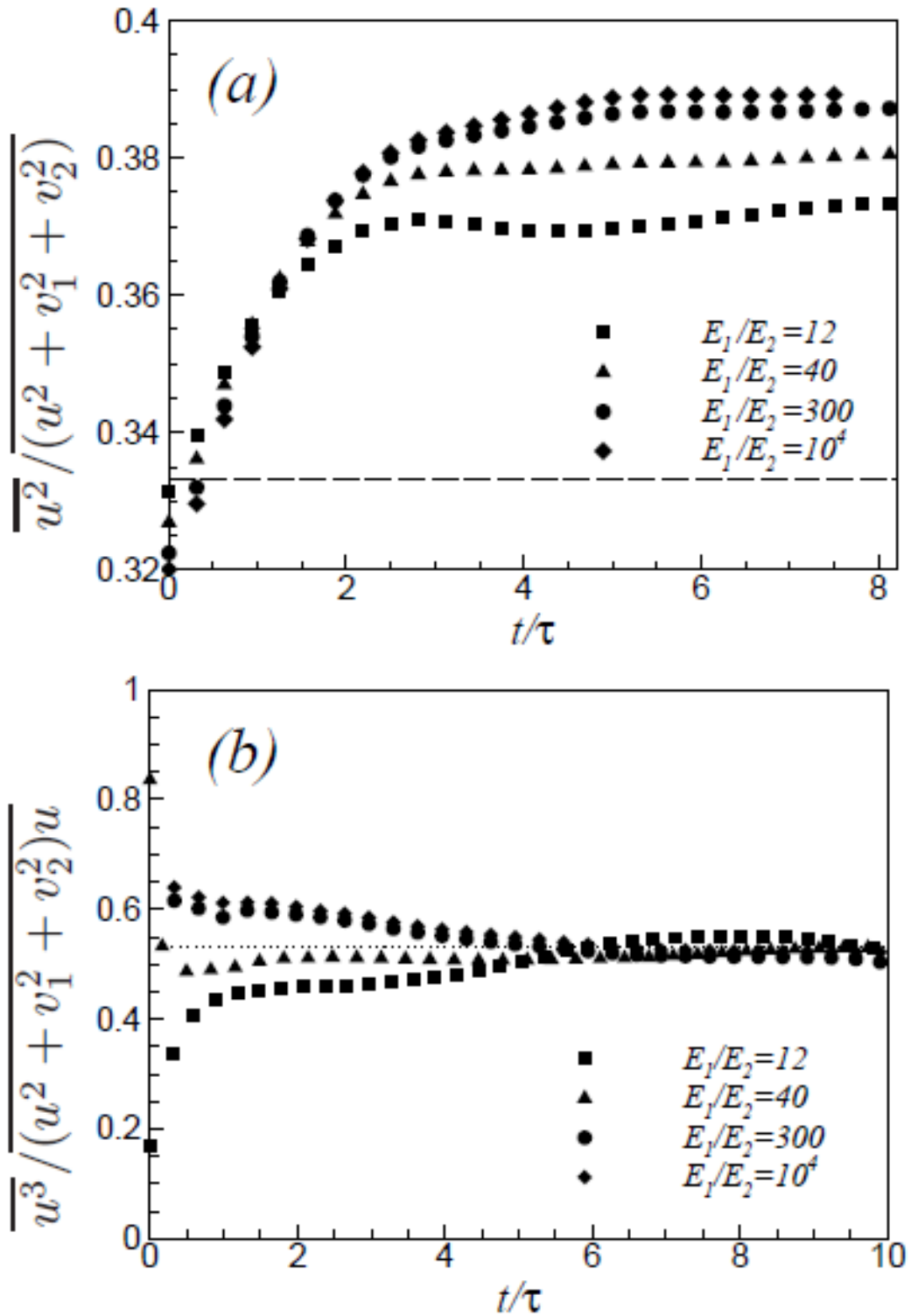
Figure 4.8. Anisotropy of the second and third moments in the mixing layer. For the second order moment in a) the dashed line marks the isotropic value of 0.33 from which the simulation starts. In the case of the third order moment b) the initial value is undefined, here the dotted line marks the asymptotic estimate.

Conclusions

The energy balance in sheared and shearless flow configurations has been considered.

Laminar and turbulent channel flows though a channel with a cavity on one wall have been numerically investigated. The velocity, pressure and kinetic energy properties in the whole domain and along the mouth of the cavity were analysed. It was seen that the momentum exchange between the cavity and the channel is directly proportional to the Reynolds number of the flow. The kinetic energy and pressure increase with Reynolds number, but with an exponent of 1.4.

On increasing the Reynolds number from low, almost Stokes flow values, the mean principal eddy dominating the dynamics of the internal cavity flow is seen to tend, at higher Reynolds, to a steady position in the downstream half of the cavity. As the Reynolds number is increased this principal eddy increases strength as more kinetic is present in the shear layer, and in doing so has a greater effect upon the pressure field in and around the cavity, inducing a pressure low at its centre.

The mean dynamics of the laminar and turbulent cavity flows for the large Reynolds number simulations has been shown to have similar effects upon the balance of energy in this flow, with an asymptotic limit found for the ratio of the mean pressure and kinetic energy transports across these two flow regimes. A link has been found between the transports of energy, in the form of pressure and in the form of kinetic energy, which permits a relatively simple study to offer some insight into the dynamics and consequences, in more complex compressible and/or acoustic studies of the topic. The asymptotic state is reached in the Reynolds range where unsteadiness, noise emission and transition to turbulence are expected to first appear. Indeed on calculating the local cavity Reynolds number, the range $169 < Re_{cavity} < 1176$ was defined where unsteadiness and transition develops.

The energy balance has also been analysed for the fluctuating part of the flow for the turbulent cavity case. In both the channel and cavity the results can be seen to agree well with previously published results for flows with recirculation zones, such as bluff body flow and backsteps. Within the recirculating zones of the cavity the pressure transport was seen to be non negligible compare to the kinetic energy transport, whereas in the channel, where the flow is uni-directional, the pressure transport is dominated by the kinetic energy transport. It was seen that the pressure transport at the cavity mouth for this sheared flow is not however dominated by the kinetic energy transport, and was found to be 0.58 its value.

A turbulent configuration lacking shear was then considered: the shearless turbulent mixing of two homogeneous isotropic turbulent fields, differing only in the energy content. This configuration can be considered to be the simplest kind of turbulent mixing. The mixing is without a gradient of scale or a mean flow, and thus no production of kinetic energy. Despite this, when varying the energy ratio over the mixing, and still maintaining equal scale, a departure of the velocity statistics from a Gaussian state was observed. This showed for the first time that a lack of kinetic energy production and scale ratio is not a sufficient condition to inhibit turbulent intermittence. Indeed the intermittence is characterized by strong bursts of velocity penetrating across the mixing, shown by the high values of skewness and kurtosis in the velocity statistics. Indeed an asymptotic limit of the level of intermittence has been found. The development of anisotropy in the third and fourth moments has also been presented.

On considering the energy balance of this configuration it was shown that the kinetic energy transport across the mixing is countered by a none negligible pressure transport. The pressure transport acts in the opposite sense and with a magnitude 0.37 of the kinetic energy transport.

Considering together the turbulent flows investigated here we see the underlying reasons for the differing energy balance. The cavity can be seen as a sheared mixing between two volume differing in energy content, the energy ratio for this cavity flow was determined to be $E_1/E_2=15.39$. The shearless mixing considered energy ratios in the range $E_1/E_2 \in (1, 10^6)$. Moving from the shearless mixing to the sheared cavity flow the ratio of transports increases from 0.37 to 0.58, owing to the added recirculatory flow as a result of the increased inter-molecular activity. Thus the recirculation increases the rolw played by pressure transport in the energy balance.

Acknowledgements

Bibliography

Abbà, A., Bonaventura, L., (2008). *A mimetic finite difference discretization for the incompressible Navier-Stokes equations.* Int. J. for Num. Meth. In Fluids, 56, pp. 1101-1106.

Armaly, B. F., Durst, F., Pereira, J. C. F., Schönung, B., (1983). Experimental and theoretical investigation of backward-facing step flow. J. Fluid Mech., 127, pp. 473-496.

Bailey, P. R., (2006). *Shearless turbulent mixing.* In: Science and Computing in Europe, A HPC-Europa publication, edited by Paola Alberigo, Giovanni Erbacci & Francesca Garofalo. ISBN 88-86037-17-1.

Bailey, P. R., Abbà, A., Tordella, D., (2008). *Pressure and kinetic energy transport across the mouth of laminar cavity flows.* 61st Annual Meeting of the American Physical Society, Fluid Dynamics Division (APS-DFD). November 23-25, 2008, San Antonio, Texas, USA. Abstract in Bull. Am. Phys. Soc., 53, pp. 204.

Batchelor, G. K., (1953). *The Theory of Homogeneous Turbulence.* Cambridge, Cambridge University Press.

Batchelor, G. K., (1990). *Fluid Dynamics.* Cambridge, Cambridge University Press.

Briggs, D. A., Ferziger, J. H., Koseff, J. R., & Monismith, S. G., (1996). *Entrainment in a shear-free turbulent mxing layer.* J. Fluid Mech., 310, pp. 215-241.

Camussi, R., Guj, G., Ragni, A., (2006). *Wall pressure fluctuations induced by turbulent boundary layers over surface discontinuities.* J. Sound & Vibration, 294, pp. 177-204.

Chiang, T. P., Sheu, T. W. H., (1999). *A numerical revisit of backward-facing step flow problem.* Phys. Fluids, 11, (4), pp. 862-874.

Colonius, T., (2001). *An overview of simulation, modeling, and active control of flow/acoustic resonance in open cavities.* AIAA 2001-0076.

Colonius, T., Lele, S. K., (2004). *Computational aeroacoustics: progress on nonlinear problems of sound generation.* Progress in Aerospace Sciences, 40/6, pp. 345-416.

Davis, T. A., Duff, I. S., (1997). *An unsymmetric-pattern multifrontal method for sparse LU factorization.* SIAM J. on Matrix Analysis and Applications, 18/1, pp. 140-158.

De Roeck, W., Desmet, W., Baelmans, M., Sas, P., (2004). *On the prediction of near-field cavity flow noise using different CAA techniques.* Proceedings of ISMA 2004., pp. 369-385.

Djenidi, L., Elavarasan, R., Antonia, R. A., (1999). *The turbulent boundary layer over transverse square cavities*. J. Fluid Mech., 395, pp. 271-294.

Fadlun, E. A., Verzicco, P., Orlandi, P., Mohd-Yusof, J., (2000). *Combined Immersed Boundary Finite Difference method for Three-Dimensional Complex Flow Simulation*. J. Comp. Physics, 161, pp. 35-60.

Giannetti, F., Luchini, P., (2007). Structural sensitivity of the first instability of the cylinder wake. J. Fluid Mech., 581, pp. 167-197.

Gilbert, B., (1980). *Diffusion mixing in grid turbulence without mean shear*. J. Fluid Mech., 100, pp. 349-365.

Grace, S. M., Dewar, W. G., Wroblewski, D. E., (2004). *Experimental investigation of the flow characteristics within a shallow wall cavity for both laminar and turbulent upstream boundary layers*. Expts. In Fluids, 36, pp. 791-804.

Hinze, J. O., (1987). *Turbulence*. New York, M^{c}graw-Hill.

Howe, M. S., (1997). *Edge, cavity and aperture tones at very low Mach numbers*. J. Fluid Mech, 330, pp. 61-84.

Howe, M. S., (2004). *Mechanism of sound generation by low Mach number flow over a wall cavity*. J. Sound & Vibration, 273, pp. 103-123.

Iovieno, M., Bailey, P. R., Tordella, D., (2006). *The intermediate asymptotics of turbulent diffusion*. 6th Euromech Fluid Mechanics Conference (EFMC6). June 26-30, 2006, Stockholm, Sweden. Abstract in EFMC6 KTH Electronic version, Abstracts Volume 2.

Iovieno, M., Cavazzoni, C. & Tordella, D., (2001). *A new technique for a parallel dealiased pseudospectral Navier-Stokes code*. Comp. Phys. Comm. J., 141, pp. 365-374.

Kang, H. S., Chester, S., Meneveau, C., (2003). *Decaying turbulence in an active-grid-generated flow and comparisons with large-eddy simulation*. J. Fluid Mech. 480, pp. 129-160.

Kang, H. S., Meneveau, C., (2008). *Experimental study of an active grid-generated shearless mixing layer and comparisons with large-eddy simulation*. Phys. Fluids, 20, (12), /125102.

Kim, J., Moin, P., (1985) *Application of a fractional step method to incompressible Navier-Stokes equations*. J. Comp. Phys., 59, pp. 308-323.

Knaepen, B., Debliquy, O. & Carati, D., (2004). *Direct numerical simulation and large-eddy simulation of a shear-free mixing layer*. J. Fluid Mech. 414, pp. 153-172.

Krishnamurty, K., (1956). *Sound radiation from surface cutouts in high speed flow.* PhD thesis, California Institute of Technology.

Le, H., Moin, P., Kim, J., (1997). *Direct numerical simulation of turbulent flow over a backward-facing step.* J. Fluid Mech., 330, pp. 349-374.

Leonardi, P., Orlandi, P., Djenidi, L., Antonia, R. A., (2004). *Structure of turbulent channel flow with square bars on one wall.* J. Heat and Fluid Flow, 25, pp. 384-392.

Leonardi, P., Orlandi, P., Smalley, R. J., Djenidi, L., Antonia, R. A., (2003). *Direct numerical simulations of turbulent channel flow with transverse square bars on one wall.* J. Fluid Mech., 491, pp. 229-238.

Lund, S. T., Wu, X., Squires, K. D., (1998). Generation of turbulent inflow data for spatially developing boundary layer simulations. J. Comp. Phys., 140, pp. 233-258.

Mansour, N. N., Kim, J., Moin, P., (1989). *Near-wall turbulence modeling.* AIAA J. 27, 1068.

Morris, P. J., (2007). *Short course in General and Computational Aeroacoustics.* 24-26th May 2007, Universita degli Studi Roma Tre, Rome.

Moser, R. D., Kim, J., Mansour, N. N., (1999). Direct numerical simulation of turbulent channel flow up to Re_tau=590. Phys. Of Fluids, 11, pp. 943-945.

Moser, R. D., Kim, J., Mansour, N. N., (1999). DNS data for turbulent channel flow. http://turbulence .ices.utexas.edu/MKM_1999.html

Mittal, R., Iaccarino, G., (2005). Immersed boundary methods. Annu. Rev. fluid Mech., 37, pp. 239-261.

Obi, S., Nakatani, H., (2001). *Modeling the turbulent transport behind a bluff body.* Proceedings of the 16th Symposium on Numerical Simulation of Turbulence. 2001, Tokyo, Japan.

Peskin, C. S., (1972). *Flow patterns around heart valves: A digital computer method for solving the equations of motion.* PhD thesis, Albert Einstein College of Medicine.

Peskin, C. S., (2002). *The immersed boundary method.* Acta Numerica, 11, pp. 1-39.

Rowley, C. W., Williams, D. R., (2006). *Dynamics and Control of High-Reynolds-Number Flow over Open Cavities.* Annu. Rev. Fluid Mech., 38, pp. 251-276.

Sarohia, V., (1977). *Experimental Investigation of oscillations in flows over shallow cavities.* AIAA J., 15, pp. 984-991.

Sinha, S. N., Gupta, A. K., Oberai, M. M., (1982). *Laminar Separating Flow over Backsteps and Cavities Part II: Cavities*. AIAA J., 20, pp. 370-375.

Shankar, P. N., Deshpande, M. D., (2000). *Fluid Mechanics in the Driven Cavity*. Annu. Rev. Fluid Mech. 32, pp. 93-136.

Suponitsky, V., Avital, E., Gaster, M., (2005). *On three-dimensionality and control of incompressible cavity flow*. Phys. Fluids, 17, 104103/1-19.

Taneda, S., (1979). *Visualisation of separating Stokes flows*. J. Phys. Soc. Japan, 46, pp. 1935-1942.

Terracol, M., Manoha, E., Herrero, C., Labourasse, E., Redonnet, S., Sagaut, P., (2005). *Hybrid methods for air frame noise numerical prediction*. Theor. Comput. Fluid Dyn., 19, pp. 197-227.

Theofilis, V., Duck, P. W., Owen, J., (2003). *Viscous linear stability analysis of rectangular duct and cavity flows*. J. Fluid Mech., 505, pp. 249-286.

Tordella, D., Iovieno, M., (2006). Numerical experiments on the intermediate asymptotics of shear-free turbulent transport and diffusion. J. Fluid Mech., 549, pp. 429-441.

Tordella, D., Iovieno, M., (2006). *The dependence on the energy ratio of the shear-free interaction between isotropic turbulences*. Direct and Large-eddy Simulation VI. Proceeding of the International ERCOFTAC workshop on direct and large-eddy simulation. September 12-14, 2005, Poitiers, France. pp. 293-300 Springer.

Tordella, D., Iovieno, M., Bailey, P. R., (2007). *Asymptotic behaviour of the shearless turbulent kinetic energy mixing*. Advances in turbulence XI. Proceedings of the 11th Euromech European Turbulence Conference (ETC11). June 25-28, 2007, Porto, Portugal. pp. 697-699 Springer.

Tordella, D., Iovieno, M., Bailey, P. R., (2007). *Asymptotic behaviour of the shearless turbulence mixing*. 13th AIAA/CEAS Aeroacoustics Conference. May 21-23, 2007, Rome, Italy. AIAA-2007-3718/1-6.

Tordella, D., Iovieno, M., Bailey, P. R., (2008). *Sufficient condition for Gaussian departure in turbulence*. Phys. Rev. E, Vol 77 016309/1-10.

Tordella, D., Iovieno, M., Bailey, P. R., (2007). *Transversal and longitudinal velocity derivative statistics in shearless turbulence*. 60th Annual Meeting of the American Physical

Society, Fluid Dynamics Division (APS-DFD). November 18-20, 2007, Salt Lake City, Utah, USA. Abstract in Bull. Am. Phys. Soc., 52 (17), November 2007.

Tritton, D. J., (1984). *Physical Fluid Dynamics*. Cambridge, Cambridge University Press.

Veeravalli, S. & Warhaft, Z., (1989). *The shearless turbulence mixing layer*. J. Fluid Mech., 207, pp. 191-229.

Wray, A. A., (1998). *Decaying isotropic turbulence in a selection of test cases for the validation of Large-Eddy Simulations of turbulent flows*. HOM02, pp. 63-64. AGARD-AR-345.

Yao, H., Cooper, R. K., Raghunathan, S., (2004). *Numerical Simulation of Incompressible Laminar Flow over Three-Dimensional Rectangular Cavities*. J. Fluids Eng. 126, pp. 919-927.

Yao, Y. F., Thomas, T. G., Sandham, N. D., Williams J. J. R., (2001). *Direct numerical simulation of turbulent flow over a rectangular trailing edge*. Theor. Comput. Fluid Dyn. 14, pp. 337-358.

Yoshizawa, A., (2002). *Statistical analysis of mean-flow effects on the pressure-velocity correlation*. Phys. Fluids, 14(5), pp. 1736-1744.

Yoshizawa, A., (1982). *Statistical evaluation of the triple velocity correlation and the pressure-velocity correlation in shear turbulence*. J. Phys. Soc. Japan, 51, pp. 2326-2337.